

ÉCOLE POLYTECHNIQUE FÉDÉRALE DE LAUSANNE
& UNIVERSITÄT BASEL

MASTER THESIS

**Spontaneous Parametric Down-Conversion
Heralded Single-Photon Source for
Quantum Memory Applications**

Author:

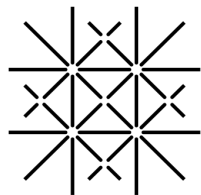
Björn COTTING

Supervised by:

Prof. Dr. Christophe GALLAND & Prof. Dr. Philipp TREUTLEIN

April 16, 2021

EPFL



**Universität
Basel**

Abstract

In this thesis the experimental realization and characterization of a robust source of heralded single photons emitted at the ^{87}Rb D₁ line (795 nm) with a narrow bandwidth of 373(1) MHz is reported. The generation process is based on type-II non-degenerate spontaneous parametric down-conversion in a periodically poled monolithic optical parametric oscillator. Potassium titanyl phosphate crystals are widely used as suitable candidates for quasi phase-matching. To achieve the target frequency, a poling period of 10.1 μm is needed. Thanks to high efficient coupling, anti-reflex coatings and reducing optics in the signal arm, heralding efficiencies $\eta_{\text{heralded}} = 53(5)\%$ were achieved. The source is operated far below threshold and maintains a second-order correlation function $g_c^{(2)} < 0.01$ up to pair generation rates of 7.5×10^5 pairs/s. In contrast to down-converted light, the pump light does not resonate in the cavity due to the absence of a high reflective dielectric coating on one crystal facet, thus providing a double pass pump scheme. In this configuration gray-tracking induced crystal deterioration is strongly suppressed. Even without recycling the pump light, photon pair rates of 5.1×10^3 pairs/(s mW) were detected. To reduce shifts in the pump frequency a sideband offset lock onto a transmission spectrum of a reference cavity has been implemented. The passively stable reference cavity shows frequency drifts of less than 10 MHz/h.

Contents

Abstract	I
Table of Contents	III
Introduction	2
1 Theory	4
1.1 Optical Prerequisites	4
1.1.1 Maxwell's Equations in Matter	4
1.1.2 Dispersion and Birefringence	5
1.1.3 The Nonlinear Polarization Vector	6
1.2 Difference Frequency Generation	8
1.3 Spontaneous Parametric Down-Conversion	10
1.4 Phase-Matching	12
1.4.1 Birefringent Phase-Matching	12
1.4.2 Quasi Phase-Matching	14
1.5 Influence of Cavity Mode Structure on OPO Tuning	15
1.6 Correlation Functions	17
2 Doubly Resonant Monolithic OPO with Double Pass Pump Scheme	20
2.1 Setup	20
2.1.1 ppKTP Crystal	21
2.1.2 Sideband Offset Lock	22
2.2 Difference Frequency Generation	22
2.3 Crystal Characterization Measurements	23
2.4 Reference Cavity Characterization Measurements	25
2.5 Heralding Efficiency	27
2.6 Second-Order Correlation Measurements	28
2.7 Backward Emitted Photons	31
3 Discussion & Conclusion	34
Acknowledgments	36
Bibliography	42
Appendix A Ray Transfer Matrix Analysis for Cavity Mode-Matching	44
Appendix B Refractive Indices of KTP	49
Appendix C Crystal Properties of KTP	50

Introduction

Since the discovery of quantum mechanics in the early twentieth century as a microscopic world governed by laws that challenge our classical intuition, there has been tremendous interest in understanding its fundamentals. With the discovery of the laser in the sixties [1], the field became much more accessible to experimentalists. Since then, researchers developed a versatile toolbox for quantum optics experiments. Theories of the effects based on quantum entanglement and quantum superposition among other non-classical features could be validated because of human creativity and persistence in experimenting in this field [2, 3]. The technologies exploiting these concepts range from quantum information and computation [4] to quantum metrology [5] and quantum key distribution (QKD) [6], which all underwent fast development from fundamental discovery to experimental proof and some even towards marketability (e.g. *ID Quantique* [7] and *MagiQ Technologies* [8] for QKD, *Qnami* [9] for quantum sensors).

These recent quantum technologies all rely on quantum bits, or qubits, which exhibit, in contrast to a classical bit, not only states 0 and 1 but every superposition of them. Even though they differ in their physical implementation, they are fundamentally grouped into two principal classes – flying and stationary qubits. Prior refers to qubits that can be sent, such as those encoded on a photon’s polarization, where as the latter are fully bound to the laboratory. Quantum computers, as one of the flagships of modern research, rely on the interconversion of stationary and flying qubits to perform any computation [10]. A viable quantum node to enable such conversion is the quantum memory. They are one of the backbones for many recent quantum technologies and show high potential for future large-scale technologies. Alongside quantum repeaters [11], they are key components of quantum networks, enabling quantum cryptography networks [12] allowing for unconditionally secure communication [13] or large scale quantum computers and simulators which help to exponentially improve computing performance for intricate problems [14, 15]. Quantum memories allow to store quantum information and to retrieve it on-demand. However, there are a manifold of possible implementations for quantum memories, all striving to find a good compromise of storage efficiency, storage time, noise level, and experimental complexity [16, 17]. Among photonic quantum memories are those based on nitrogen-vacancy center in diamond [18, 19], crystals doped with rare earths [20, 21] or trapped ions [22], single atoms [23] and cold atomic gases [24, 25] as well as hot alkali vapor memories [26, 27]. Latter come in a variety of implementations but generally benefit from high storage efficiencies and can usually be operated outside cryogenic temperatures, and are therefore chosen as an easy to implement option for a proof of principle for large scale applications. However, it is crucial for quantum memories to be matched with an adequate source of single-photons: first of all, memories require a certain target frequency of the single photons, second the bandwidth is to be matched, and third the extraction rate or heralding efficiency need to be high enough to surpass the readout noise. Finally, the photon rates need to be high enough to obtain statistics in order to quantify the memories’ performance.

Single-photon sources are regarded to be the workhorse of most modern photonics based quantum experiments and applications and hence pose a crucial task for today’s research and industry. Their nature inherently allows them to reliably generate quantum states which can be used for quantum processing. Single-photon sources are designed to emit highly indistinguishable photons [28–30] or pairs with a high degree of entanglement [31, 32]. Further on the wish list for single photon sources are quantum state purity, extraction efficiency, and on-demand generation. Two of today’s most advanced standards for single-photon sources each partially fulfill these requirements: semiconductor quantum dots (QD) [33–37] and sources based on spontaneous parametric down-conversion (SPDC) [38–42]. The latter are the focus of this work. SPDC sources are generally subject to contamination of higher photon number states and thus need to be run with a low generation probability per coherence time p , that is in a pump regime far below threshold. Therefore, when needing an N -photon state, the probabilistic nature of the sources decrease the generation rate rapidly for high N as the success probability scales exponentially as $P \propto p^N$ [43, 44]. N -photon states are needed in multiple applications such as boson sampling [45, 46] or linear optical quantum computing [15, 47] in order to perform any calculations on photonic circuits. Combining an SPDC source with a quantum memory helps to overcome its probabilistic character and allows generation of on-demand high photon pair states.

The quantum memory we try to operate proposed by Wolters et al. [48] is in a warm Rubidium vapor with an end-to-end efficiency of $\eta_{e2e} = 3.4(3)\%$ for 50 ns storage time. In order to operate the quantum

memory, the source requirements are the following: first of all, it needs to generate photons with a tuneable emission spectrum close to the D_1 line of ^{87}Rb around 795 nm, second the memory requires broadband photons in the bandwidth range of a couple of hundreds of MHz up to 1 GHz, third the extraction efficiency should be exceeding 25% in order to obtain a sub-unity readout SNR, and finally, the herald rate should exceed 50 000 counts/s. The memory has been characterized with weak coherent pulses emulating QD photons [49] and first attempts were made to operate it with a monolithic SPDC heralded single-photon source [50]. Central element of the SPDC source is a periodically poled potassium titanyl phosphate (ppKTP) crystal equipped with highly reflective dielectric coatings for pump photons as well as the down-converted daughter photons – *signal* and *idler*. We iterated this design by omitting the pump coating on one side of the crystal, therefore enabling a pump double pass. This new design is usually referred to as *monolithic doubly resonant with a double pass pumping scheme*.

With this improvement of the a heralded single-photon source design adopted from Mottola et al. [51] we hope to improve one aspect in particular: Our new source design uses a double pass instead of a multi pass pump scheme. First, since the crystal does not form a resonator cavity for the pump light, there is no particular need for stringent mode matching. In return, we hope to find gray-tracking [52] to be significantly suppressed. Interestingly, this should also improve pair generation rates per mW since we are not restricted to off-resonant pumping anymore. On the other hand, we are unable to lock the pump laser on crystal transmission modes, but we equip the source with a tuneable sideband offset lock enabled by a reference cavity. By implementing these changes we hope to significantly improve the crystal lifetime as well as the source’s tuneability and handling.

Structure

This thesis is structured in three chapters: starting with a theory part, then proceeding with the experimental part about the doubly resonant crystal, and finally concluding with a discussion which summarizes the achievements and problems faced with this single-photon source design.

Part 1: The theory part describes the physical background necessary to explain the physics of SPDC. Herein, we start both with Maxwell’s equations as well as dispersion and birefringence in order to explain the light-matter interaction. Afterwards, we proceed with explaining and deriving a classical theory for difference frequency generation (DFG) and a semi-classical theory for SPDC for which we find respective photon generation rates. These introduce the phase-matching conditions. We then explain two ways to satisfy them: Birefringent phase-matching, which exploits the angle-dependency of the refractive indices, and quasi phase-matching, which enables phase matching without angle tuning by exploiting a periodically alternating crystal orientation. Additionally, we explain the mode structure in optical parametric oscillators (OPO) which, together with the phase-matching conditions determine the working parameters (crystal temperature and pump frequency). Finally, we describe second-order correlation functions which will help us in characterizing the single-photon source.

Part 2: In the experimental part, we first explain the experimental setup and the crystal as well as the reference cavity. Furthermore, we show the importance of the DFG mode and how it allows us to adjust parts of the setup. Thereafter, we explain the methods to verify the working parameters obtained in the theory part of the thesis. Finally, we perform correlation measurements in order to characterize the source on its single-photon character as well as its pair generation rate.

Part 3: In the final part, we discuss the problems we faced during the setup process of the source. Moreover, we summarize the results obtained during the measurements and we give an outlook on what can be done in the near future in order to improve the SPDC single-photon source.

1 Theory

Single-photon generation is a non-trivial task and requires the understanding of principles concerning linear and nonlinear optics. It is helpful to establish certain terms and concepts on the following pages before proceeding to more intricate theories. After introducing Maxwell's equations in matter, the chapter continues with a short description of the refractive index of dispersive media. The Section 1.1 closes with the introduction of the nonlinearity of the polarization vector. Thereafter, we present classical and semi-classical theories, respectively, which are necessary to describe the three wave mixing processes of DFG as well as SPDC. Finally, more specific theories are provided towards optimization and characterization as well as descriptions of the emerging quantum states of our single-photon source. The theory part of my thesis motivates the experimental procedures used in order to obtain single-photon states from a ppKTP crystal.

1.1 Optical Prerequisites

Electrodynamical and optical prerequisites are needed to establish terms and notations which are used later. These explanations and derivations can be found in standard literature about quantum optics [53–55]. Even though these are basic theories, they show high importance in later chapters since they lay the physical groundwork for more specific descriptions of single-photon extraction with SPDC. This chapter closely follows [55] and [56] with some calculations found in [57] if not specified otherwise.

1.1.1 Maxwell's Equations in Matter

It is necessary to start with the description of propagation of waves within dispersive media, which originates in Maxwell's equations. In vacuum, these equations are used to describe every electrodynamic phenomenon in the presence of an electric field $\mathbf{E}(\mathbf{r}, t)$ and a magnetic field $\mathbf{B}(\mathbf{r}, t)$. In dielectric matter, however, it is required to introduce the displacement field \mathbf{D} which accounts for the materials properties. The equations therefore read [53–55]

$$\nabla \cdot \mathbf{D} = 0, \tag{1.1.1a}$$

$$\nabla \cdot \mathbf{B} = 0, \tag{1.1.1b}$$

$$\nabla \times \mathbf{E} = -\frac{\partial \mathbf{B}}{\partial t}, \tag{1.1.1c}$$

$$\nabla \times \mathbf{B} = \mu_0 \frac{\partial \mathbf{D}}{\partial t}. \tag{1.1.1d}$$

Additionally, this particular set of Maxwell's equations accounts for no free charges ($\rho = 0$) nor currents ($\mathbf{J}=0$). Using the displacement field's definition

$$\mathbf{D} = \epsilon_0 \mathbf{E} + \mathbf{P}, \tag{1.1.2}$$

with the polarization depending on the electric susceptibility χ :

$$\mathbf{P} = \epsilon_0 \chi \mathbf{E}. \tag{1.1.3}$$

Combining both expressions yields

$$\mathbf{D} = \epsilon_0(1 + \chi)\mathbf{E} = \epsilon_0 n^2 \mathbf{E} = \epsilon \mathbf{E}. \tag{1.1.4}$$

For now we treat χ to act as a scalar so that the Gauss's law (1.1.1a) reduces to

$$\nabla \cdot \mathbf{E} = 0 \tag{1.1.5}$$

and similarly the Ampère-Maxwell law (1.1.1d) becomes

$$\nabla \times \mathbf{B} = \mu_0 \epsilon \frac{\partial \mathbf{E}}{\partial t}, \tag{1.1.6}$$

respectively. Taking the curl of both Equation (1.1.1c) and (1.1.6), we find

$$\nabla \times (\nabla \times \mathbf{E}) = \nabla \times \left(-\frac{\partial \mathbf{B}}{\partial t} \right) = -\frac{\partial}{\partial t} (\nabla \times \mathbf{B}) \stackrel{Eq.(1.1.6)}{=} -\mu_0 \epsilon \frac{\partial^2 \mathbf{E}}{\partial t^2}, \quad (1.1.7a)$$

$$\nabla \times (\nabla \times \mathbf{B}) = \nabla \times \left(\mu_0 \epsilon \frac{\partial \mathbf{E}}{\partial t} \right) = \mu_0 \epsilon \frac{\partial}{\partial t} (\nabla \times \mathbf{E}) \stackrel{Eq.(1.1.1c)}{=} -\mu_0 \epsilon \frac{\partial^2 \mathbf{B}}{\partial t^2}, \quad (1.1.7b)$$

where the vector identity

$$\nabla \times (\nabla \times \mathbf{V}) = \nabla(\nabla \cdot \mathbf{V}) - \nabla^2 \mathbf{V} \quad (1.1.8)$$

can be applied to both left-hand sides. The terms of $\nabla \cdot \mathbf{E}$ and $\nabla \cdot \mathbf{B}$ disappear due to Equations (1.1.1b) and (1.1.5). Employing the identity $c^2 = \epsilon_0 \mu_0$ yields wave equations for both \mathbf{E} and \mathbf{B}

$$\nabla^2 \mathbf{E} - \frac{1}{n^2 c^2} \frac{\partial^2 \mathbf{E}}{\partial t^2} = 0, \quad (1.1.9a)$$

$$\nabla^2 \mathbf{B} - \frac{1}{n^2 c^2} \frac{\partial^2 \mathbf{B}}{\partial t^2} = 0. \quad (1.1.9b)$$

One possible solution for the wave equation (1.1.9a) is

$$\mathbf{E} = \mathbf{E}_0 \exp(i(-\omega t + \mathbf{k} \cdot \mathbf{r})), \quad (1.1.10)$$

where the wave vector \mathbf{k} includes the refractive index n , specifically, it can be found as

$$\mathbf{k} = \frac{2\pi n}{\lambda} \hat{\mathbf{k}}. \quad (1.1.11)$$

Considering only the solution's real part, we find

$$\text{Re}(\mathbf{E}) = \mathbf{E}_0 \cos(-\omega t + \mathbf{k} \cdot \mathbf{r}). \quad (1.1.12)$$

It is convenient to describe the electric field by the complex amplitude $\mathbf{A} = \mathbf{E}_0 \exp(i\phi)$:

$$\mathbf{E} = \frac{1}{2} \left(\mathbf{A} \exp[i(-\omega t + \mathbf{k} \cdot \mathbf{r})] + \text{c.c.} \right) \quad (1.1.13)$$

The complex conjugate ensures that the electric field remains real-valued.

1.1.2 Dispersion and Birefringence

The index of refraction is an intricate but crucial quantity of a crystal. It does not solely alter the wavevector but can also be held responsible for refraction, the chromatic splitting of the light into its frequency components on surfaces, as well as influencing the wave's group velocity. The latter is wavelength dependent and behaves according to

$$v(\lambda) = \frac{c}{n(\lambda)}. \quad (1.1.14)$$

Propagation speeds, however, do not only depend on the light's wavelength but also on its polarization and propagation direction. This effect is described by the Sellmeier equations. A particular expression for KTP crystals is given by [58]:

$$n(\lambda)^2 = A + \frac{B}{1 - C/\lambda^2} + \frac{D}{1 - E/\lambda^2} + F\lambda^2, \quad (1.1.15)$$

where the coefficients A to F are determined empirically. The Sellmeier equations do not have a universal shape but, depending on material and crystal axis, show more or fewer coefficients, oftentimes depending on temperature. Especially for non-isotropic materials they depend greatly on the respective crystal axes since the crystal structure is either not cubic or distorted by one of many mechanisms triggering *birefringence*. It is therefore not surprising that the linear electric susceptibility $\chi^{(1)}$ becomes a tensor

with diagonals as refractive indices for every axis. Crystals with different refractive indices with respect to every principal axis ($n_x \neq n_y \neq n_z$) are then referred to as *biaxial*. Other crystals with two (three) equal indices are called *uniaxial (isotropic)*.

Let us assume light propagation within a uniaxial crystal, where there is always one axis which yields a rotation axis so that the refractive index stays unchanged – the *optical axis*. In other words, light propagating along the optical axis, whose polarization is perpendicular (by definition) to its propagation direction, is characterized by an *ordinary refractive index* n_o , regardless of its specific polarization. However, for every other propagation direction, the polarization of the wave can be split into two parts. One part would be within the plane perpendicular to the optical axis and thus governed by the ordinary refractive index. This ray is often denoted as *ordinary ray*. The other part of the beam not lying within this plane, therefore not exposed to the material's ordinary refractive index, is called the *extraordinary ray*. Unlike the ordinary ray its refractive index is direction dependent.

This can be visualized by a simple example: Assume unpolarized light enters a uniaxial birefringent medium so that it immediately splits into two beams. The opposing polarization are carried by the ordinary and the extraordinary ray. Prior is fully exposed to the ordinary refractive index where as the latter is governed by the *effective refractive index* $n_{\text{eff}}(\theta, \lambda, T)$. This refractive index lies between the ordinary and the *extraordinary refractive index* n_e , depending on the ray direction θ (see Figure 1, right), given by the index ellipsoid in Figure 1, according to:

$$\frac{1}{n_{\text{eff}}(\theta, \lambda, T)^2} = \frac{\cos^2 \theta}{n_o(\lambda, T)^2} + \frac{\sin^2 \theta}{n_e(\lambda, T)^2}. \quad (1.1.16)$$

As expected, once θ approaches zero we find the effective refractive index to coincide with the ordinary refractive index. Furthermore, the difference between n_e and n_o classifies uniaxial crystals according to

$$\Delta n = n_e - n_o, \quad (1.1.17)$$

into a positive ($n_e > n_o$) or negative ($n_e < n_o$) birefringence. For the positive (negative) case the polarization of the fast (slow) wave is perpendicular to the optical axis.

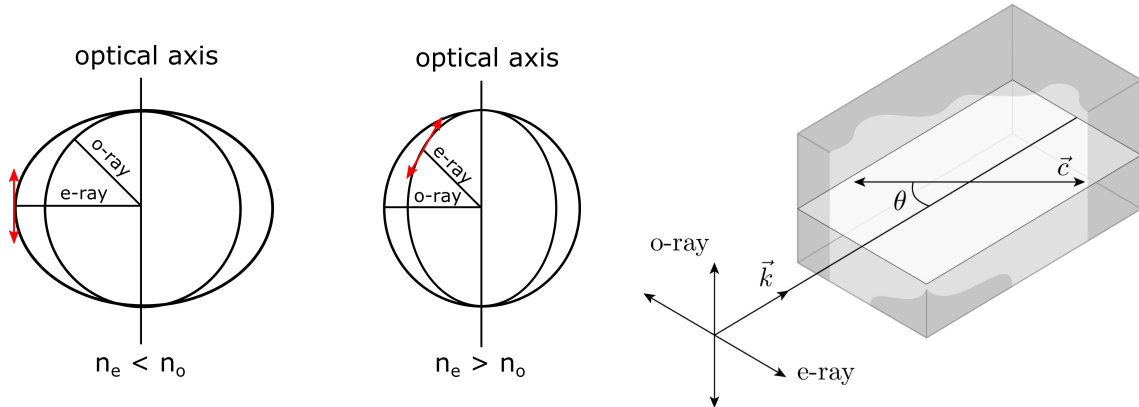


Figure 1: Left: Effective refractive index's $n_{\text{eff}}(\theta, \lambda, T)$ dependency on ordinary and extraordinary refractive indices, n_o and n_e shown graphically (left). Uniaxial crystals show either positive ($n_e > n_o$) or negative ($n_e < n_o$) birefringence. Right: Representation of angle θ between propagation direction and optical axis (reproduced from [55]).

1.1.3 The Nonlinear Polarization Vector

So far the polarization density vector \mathbf{P} has been used according to the definition in section 1.1.1 but without going into detail about the electric susceptibility χ . By including higher order terms of χ in Equation (1.1.3) we find the polarization to be

$$\begin{aligned}\mathbf{P} &= \epsilon_0\chi^{(1)}\mathbf{E} + \epsilon_0\chi^{(2)}\mathbf{E}^2 + \epsilon_0\chi^{(3)}\mathbf{E}^3 + \dots \\ &= \mathbf{P}^{(1)} + \mathbf{P}^{(2)} + \mathbf{P}^{(3)} + \dots\end{aligned}\tag{1.1.18}$$

Hence the susceptibility can be rewritten together with Equation (1.1.3) as

$$\chi = \chi^{(1)} + \chi^{(2)}\mathbf{E} + \chi^{(3)}\mathbf{E}^2 + \dots\tag{1.1.19}$$

This definition precisely shows the dependency of higher order terms on the field strength. For low fields higher orders of \mathbf{E} become negligible and thus the susceptibility remains linear. The polarization can then easily be calculated as in Equation (1.1.3):

$$\mathbf{P} = \epsilon_0\chi^{(1)}\mathbf{E},\tag{1.1.20}$$

along with

$$n^2 = 1 + \chi^{(1)}.\tag{1.1.21}$$

For stronger fields, however, higher order terms become more significant and thus have to be taken into account. For instance, the second-order term $\chi^{(2)}$ enables three wave mixing phenomena and the third-order term $\chi^{(3)}$ leads to four wave mixing. SPDC is a $\chi^{(2)}$ process which requires the lowest order nonlinear susceptibility term which is according to (1.1.18):

$$\mathbf{P}^{(2)} = \epsilon_0\chi^{(2)}\mathbf{E}^2.\tag{1.1.22}$$

The second-order nonlinear polarization vector can be rewritten as the sum over the entries of the electric susceptibility as

$$\mathbf{P}_i^{(2)} = \epsilon_0 \sum_{jk} \chi_{ijk}^{(2)} E_j E_k\tag{1.1.23}$$

where E_j and E_k are field amplitudes involved in the three wave mixing processes as introduced in Equation (1.1.13). Fortunately, due to crystal symmetries, we do not have to determine all 81 entries of the tensor $\chi^{(2)}$ but it is significantly more intricate than for the first-order term. In fact, Kleinman [59] defined symmetry relations generally applicable for any crystal lattices which reduce the entries to only 18 for the second-order term. Moreover, it is advantageous to use a reduced notation to allow the rewriting of the nonlinear susceptibility in terms of nonlinear coefficients d_{im} which inherently respect the symmetries. The expression of Equation (1.1.23) encompasses many processes such as second harmonic generation, sum frequency generation or optical rectification. Another $\chi^{(2)}$ mechanism is difference frequency generation (DFG) which down-converts one higher energy photon into two lower energy daughter photons. Its corresponding polarization vector, expressed in the Kleinman symmetry, is given by

$$\mathbf{P}_i^{(2)}(\omega_n - \omega_m) = 2\epsilon_0 \sum_{jk} \sum_{mn} d_{ijk} E_j(\omega_n) E_k(\omega_m)^*.\tag{1.1.24}$$

Since, in some cases, many entries of d_{ijk} do not enter the calculation, we can define a scalar denoted as *effective nonlinear optical coefficient* d_{eff} for the required process. For the case of DFG the expression of Equation (1.1.24) simplifies to the scalar relationship:

$$P(\omega_3) = 4\epsilon_0 d_{\text{eff}} E(\omega_1) E(\omega_2)^*.\tag{1.1.25}$$

By comparing Equations (1.1.25) and (1.1.23) we find that for DFG the relation of the electric susceptibility and the effective nonlinear optical coefficient is

$$d_{\text{eff}} = \chi^{(2)}/4.\tag{1.1.26}$$

1.2 Difference Frequency Generation

The SPDC process is a second-order nonlinear optical process for which a single incident light field decays spontaneously into two fields. Since the process involves only a single coherent input field decaying into two coherent output fields, it has to be matched with vacuum fluctuation so that a semi-classical or quantum input-output theory has to be implemented [60–62]. DFG on the other hand describes in principal the same $\chi^{(2)}$ -process but provides two coherent input fields so that there is no need for an auxiliary field originating from the vacuum state. Its description can therefore be done fully classically. It is here used in order to approach the SPDC derivation and intends to give the reader a better intuition of three-wave mixing processes. DFG describes a stimulated process for which a high energy photon of frequency ω_2 decays in two daughter photons of frequency ω_1 and ω_3 as hinted at in the expression of Equation (1.1.25). The high energy photon decays in a stimulated process according to

$$\hbar\omega_p + \hbar\omega_s \rightarrow \hbar\omega_i + \hbar\omega_s + \hbar\omega_s, \quad (1.2.1)$$

where we are referring to the photons 1, 2, and 3 as *idler*, *pump*, and *signal* photons for historical reasons. Obviously, the process must comply with energy conservation so that the newly generated signal photons have frequency

$$\omega_i = \omega_p - \omega_s. \quad (1.2.2)$$

It is important to note that there are three different types of down-conversion: type-0, type-I, and type-II. The first two types are polarization degenerate, meaning daughter photons exhibit the same polarization. Specifically, for type-0 down-conversion pump and daughter photons share the same polarization where as they show orthogonal polarization for type-I. On the other hand, type-II down-converted photons are orthogonally polarized, where the pump polarization either matches the signal or the idler polarization. Type-II is often the down-conversion process of choice to generate polarization entangled photons.

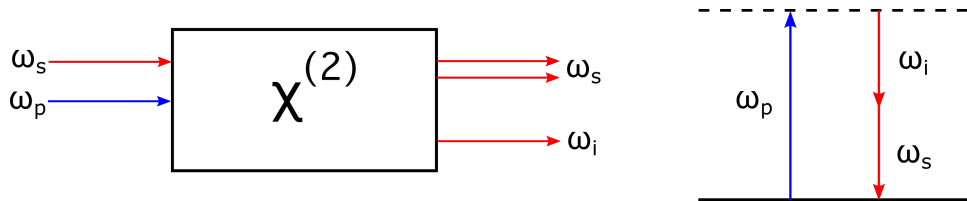


Figure 2: Schematic interpretation of DFG (left) and its energy diagram (right). The solid lines stand for coherent fields.

Equation (1.2.1) implies the amplification nature of the DFG process. In the process, the intensity of the signal field increases due to stimulated emission. For DFG we consider the nonlinear polarization vector up to second-order:

$$\mathbf{P} = \mathbf{P}^{(1)} + \mathbf{P}^{(2)}. \quad (1.2.3)$$

Higher order processes are, for now, being omitted due to the operation in a regime far below threshold. This regime refers to pump powers so low to exclude higher number pair generations such as two pair generation etc. By doing so, we can confidently assume to only have pair generation events and thus the omittance of higher order terms is justified. Considering coherent pump and signal input fields, the resulting idler field is characterized by

$$\mathbf{E}(\omega_i) = \frac{1}{2} \mathbf{A}_i \exp[i(-\omega_i t + \mathbf{k}_i \mathbf{r})] + \text{c.c.} \quad (1.2.4)$$

Using this definition for the linear polarization vector of Equation (1.2.3), the first-order signal polarization vector reads

$$\mathbf{P}^{(1)}(\omega_i) = \frac{1}{2} \epsilon_0 \chi^{(1)} \mathbf{A}_i \exp[i(-\omega_i t + \mathbf{k}_i \mathbf{r})] + \text{c.c.} \quad (1.2.5)$$

Similarly we find the second-order nonlinear polarization term according to Equation (1.1.25) as

$$\mathbf{P}^{(2)}(\omega_i) = \epsilon_0 d_{\text{eff}} \mathbf{A}_p \mathbf{A}_s^* \exp[i(-\omega_i t + (\mathbf{k}_p - \mathbf{k}_s) \mathbf{r})] + \text{c.c.}, \quad (1.2.6)$$

where \mathbf{A}_s and \mathbf{A}_p are the complex field amplitudes of signal and pump, respectively. For the next step we recall Maxwell's equation introduced in Chapter 1.1.1. By applying a curl to Faraday's law (1.1.1c) we get

$$\nabla \times (\nabla \times \mathbf{E}) = \nabla \times \left(-\frac{\partial \mathbf{B}}{\partial t} \right) = -\frac{\partial}{\partial t} (\nabla \times \mathbf{B}) \stackrel{\text{Eq. (1.1.1d)}}{=} -\mu_0 \frac{\partial^2 \mathbf{D}}{\partial t^2}, \quad (1.2.7)$$

where we assume a nonmagnetic material in the last step. Using identity (1.1.8) we rewrite the expression as

$$\nabla(\nabla \cdot \mathbf{E}) - \nabla^2 \mathbf{E} = -\mu_0 \frac{\partial^2 \mathbf{D}}{\partial t^2}. \quad (1.2.8)$$

At this point we have to take into account some considerations. First, we assume similarly to Section 1.1.1 the material to be non-conductive, meaning there are no free charges ($\rho = 0$). Consequently, instead of using Maxwell's equation (1.1.1a) we can directly utilize Maxwell's equation for no free charges (1.1.5). Secondly, for o-rays in the case of an isotropic material ($n_x = n_y = n_z$) the electric field \mathbf{E} reduces to just a scalar multiple of \mathbf{D} according to Equation (1.1.4). In return, the electric field \mathbf{E} becomes divergence-free too. Moreover, we assume only a weak birefringence [56] so that \mathbf{E} and \mathbf{D} keep a similar orientation and therefore obtain $\nabla \cdot \mathbf{E} \approx 0$ in any case. This assumption let us omit the first term of Equation (1.2.8). By inserting Equation (1.1.2) the expression reads

$$\nabla^2 \mathbf{E} = \mu_0 \epsilon_0 \frac{\partial^2 \mathbf{E}}{\partial t^2} + \mu_0 \frac{\partial^2 \mathbf{P}}{\partial t^2}. \quad (1.2.9)$$

Without loss of generality we may define the propagation to be along the z-axis so that every ∇ simply becomes a $\partial/\partial z$ operation. The corresponding scalar form can then be found to be

$$\frac{\partial^2 E}{\partial z^2} = \mu_0 \epsilon_0 \frac{\partial^2 E}{\partial t^2} + \mu_0 \frac{\partial^2 P}{\partial t^2}. \quad (1.2.10)$$

Recalling the scalar field counterparts of Equations (1.2.4), (1.2.5), and (1.2.6) for the idler field and inserting them into the preceding expression yields

$$\begin{aligned} \frac{1}{2} \left(-k_i^2 A_i + 2ik_i \frac{\partial A_i}{\partial z} + \frac{\partial^2 A_i}{\partial z^2} \right) \cdot e^{i(-\omega_i t + k_i z)} = & -\frac{1}{2} \mu_0 \epsilon_0 \omega_i^2 A_i (1 + \chi^{(1)}) e^{i(-\omega_i t + k_i z)} \\ & - \mu_0 \epsilon_0 \omega_i^2 d_{\text{eff}} A_p A_s^* e^{i(-\omega_i t + (k_p - k_s) z)}. \end{aligned} \quad (1.2.11)$$

We here replaced the tensor $\chi^{(2)}/4$ with the scalar effective nonlinear coefficient d_{eff} as described in section 1.1.3. Using the *slowly varying amplitude approximation*

$$\left| \frac{\partial^2 A_i}{\partial z^2} \right| \ll \left| k_i \frac{\partial A_i}{\partial z} \right|, \quad (1.2.12)$$

allows us to cancel the third term of the left-hand side of Equation (1.2.11) and subsequently enables simplified rewriting. Furthermore, we can make use of the identity $\mu_0 \epsilon_0 = 1/c^2$ and Equations (1.1.21) and (1.1.11) to obtain

$$in_i \frac{\partial A_i}{\partial z} = -\frac{\omega_i d_{\text{eff}}}{c} A_p A_s^* e^{i\Delta k}. \quad (1.2.13)$$

This expression introduces the *phase or momentum mismatch vector*

$$\Delta k = k_p - k_s - k_i. \quad (1.2.14)$$

This helps in transforming Equation (1.2.13) into an ordinary differential equation simplifying further calculations. The integration over z yields

$$A_i = i \frac{\omega_i d_{\text{eff}}}{n_i c} A_p A_s^* I(z), \quad (1.2.15)$$

where $I(z)$ reads

$$\begin{aligned}
I(z) &= \int_0^L e^{i\Delta kz} dz \\
&= \frac{1}{i\Delta k} e^{i\Delta kz} \Big|_0^L \\
&= \frac{2}{\Delta k} e^{i\Delta kL/2} \operatorname{sinc}\left(\frac{\Delta kL}{2}\right).
\end{aligned} \tag{1.2.16}$$

The upper boundary of the integral is length L over which the light interacts with the non-linear medium and corresponds to the crystal length for our case. The total expression of the complex idler field amplitude is therefore reduced to

$$A_i = i \frac{\omega_i d_{\text{eff}}}{n_i c} L A_p A_s^* e^{i\Delta kL/2} \operatorname{sinc}(\Delta kL/2), \tag{1.2.17}$$

with $\operatorname{sinc}(x) = \sin(x)/x$. The complex field amplitude cannot be determined with any measurement directly. But we can convert it to an observable such as the field intensity I . The idler field intensity is given by the magnitude of the time-averaged Poynting vector [56], given by

$$I = \frac{n}{2\mu_0 c} |A|^2. \tag{1.2.18}$$

Inserting the complex field amplitude into this intensity expression, we obtain

$$I_i = \frac{\omega_i^2 d_{\text{eff}}^2}{2\mu_0 n_i c^3} L^2 |A_p|^2 |A_s|^2 \operatorname{sinc}^2\left(\frac{\Delta kL}{2}\right). \tag{1.2.19}$$

Replacing the complex amplitudes of pump and signal fields with the help of Equation (1.2.18), the idler intensity simplifies to

$$I_i = \frac{2\mu_0 \omega_s^2 d_{\text{eff}}^2}{n_p n_s n_i c} L^2 I_p I_s \operatorname{sinc}^2\left(\frac{\Delta kL}{2}\right). \tag{1.2.20}$$

It is important to note that the intensity of the idler field is linearly proportional to both pump and signal fields as well as proportional to the distance traveled by the light within the medium squared. The sinc-function reaches its maximum at zero, leading to highest intensities at zero wavevector mismatch. With higher momentum mismatches the signal intensity decreases rapidly. This becomes more evident in a discussion later within this section.

1.3 Spontaneous Parametric Down-Conversion

As claimed in the previous chapter, processes with a single coherent input field such as spontaneous parametric down-conversion cannot be treated purely classically. However, its similarity to DFG allows us to take an analogous description. By replacing the signal field with vacuum fluctuations as depicted in Figure 3 we directly force quantum-mechanical operators onto the classical approach. Despite operators now introducing some quantum-mechanics, its framework remains classical. Unsurprisingly, the approach is therefore denoted as the *semi-classical* description. We find the newly defined quantum-mechanical field operators to be separated into negative and positive field operators,

$$\mathbf{E} = \mathbf{E}^+ + \mathbf{E}^-. \tag{1.3.1}$$

Its components are given by the field quantization theory as [53]

$$\mathbf{E}^+ = i \sum_{\mu=\pm 1} \int_0^\infty \sqrt{\frac{\hbar\omega}{2\epsilon_0 n(\omega) V_q}} (a^{(\mu)}(\mathbf{k}) e^{i(\omega t + \mathbf{k}(\omega)\mathbf{r})}) d\omega, \quad (1.3.2a)$$

$$\mathbf{E}^- = -i \sum_{\mu=\pm 1} \int_0^\infty \sqrt{\frac{\hbar\omega}{2\epsilon_0 n(\omega) V_q}} (a^{(\mu)\dagger}(\mathbf{k}) e^{-i(\omega t + \mathbf{k}(\omega)\mathbf{r})}) d\omega, \quad (1.3.2b)$$

with quantization volume V_q . The quantum-mechanical creation and annihilation operators $a^{(\mu)\dagger}(\mathbf{k})$, $a^{(\mu)}(\mathbf{k})$ acting on photons with polarization μ and momentum \mathbf{k} and obey common bosonic commutations relations:

$$[a^{(\mu')}(\mathbf{k}'), a^{(\mu)\dagger}(\mathbf{k})] = \delta_{\mathbf{k}'\mathbf{k}} \delta_{\mu'\mu} \quad \text{and} \quad [a^{(\mu')}(\mathbf{k}'), a^{(\mu)}(\mathbf{k})] = [a^{(\mu')\dagger}(\mathbf{k}'), a^{(\mu)\dagger}(\mathbf{k})] = 0. \quad (1.3.3)$$

In future references the frequency dependence of annihilation and creation operators, refractive indices, and wave vectors will not be written explicitly. Let us now consider a monochromatic plane wave for the signal which conveniently omits the integration over frequency ω in (1.3.1) and so that

$$\mathbf{E} = i\mathcal{E}(a^{(\mu)} e^{i(-\omega t + \mathbf{k}\mathbf{r})} - a^{(\mu)\dagger} e^{-i(-\omega t + \mathbf{k}\mathbf{r})}), \quad (1.3.4)$$

where \mathcal{E} takes into account all terms under the square root. Comparing coefficients after application onto the vacuum state $|0\rangle$ together with the classical field operator introduced in the previous subsection (1.2.4) yields the signal field amplitude

$$\begin{aligned} A_s^* &\leftrightarrow -2i\mathcal{E}_s a^{(\mu_s)\dagger}(k_s) |0\rangle \\ &\leftrightarrow -2i\mathcal{E}_s |\mathbf{k}, \mu\rangle_s, \end{aligned} \quad (1.3.5)$$

where we again consider propagation direction along the z-axis for simplicity. The quantum state $|\mathbf{k}, \mu\rangle_s$ describes the one photon quantum state for a photon with wavevector \mathbf{k} and polarization μ . We need to keep in mind that for annihilation operators acting on the vacuum state $a^{(\mu)}(k) |0\rangle = 0$ applies. Using the intensity amplitude relation introduced in Equation (1.2.18) yields for the signal vacuum fluctuation:

$$I_s = \frac{2n_s |\mathcal{E}_s|^2}{\mu_0 c}. \quad (1.3.6)$$

Resubstituting \mathcal{E} and using the identity $c^2 = 1/(\epsilon_0 \mu_0)$ leads to

$$I_s = \frac{\hbar\omega_s c}{V_q} \quad (1.3.7)$$

for the vacuum signal intensity. This expression can directly replace the signal intensity of the classical solution for DFG (1.2.20) and thus characterizes the semi-classical result for the SPDC idler intensity:

$$I_{i,SC} = \frac{2\mu_0 \hbar\omega_i^2 \omega_s d_{\text{eff}}^2}{n_p n_s n_i V_q} L^2 I_p \text{sinc}^2\left(\frac{\Delta k L}{2}\right). \quad (1.3.8)$$

For obvious reasons, the signal field intensity dependence dropped so that the idler field only remains dependent on its only input, the pump field.

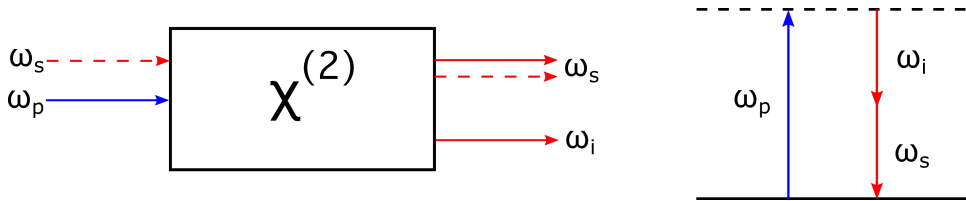


Figure 3: Schematic of SPDC; ω_p , ω_s and ω_i correspond to pump, signal and idler frequencies respectively (left) together with its energy diagram (right). Continuous lines represent coherent fields and dotted lines correspond to vacuum fluctuations.

1.4 Phase-Matching

As hinted at in the previous section, energy conservation (1.2.2) must hold for all three-wave mixing processes. However, it does not necessarily satisfy the phase-matching condition of Equation (1.2.14) simultaneously. This is because the wavevector inherently depends on the refractive index in addition to the frequency according to

$$|\mathbf{k}| = \frac{n\omega}{c}. \quad (1.4.1)$$

The refractive index not solely depends on the crystal's material but also on its lattice type and subsequently also its growth orientation. These properties impose direction and polarization dependencies onto the refractive index. The latter can be quantified according to Section 1.1.2 by defining an ordinary (extraordinary) refractive index n_o (n_e). These properties can be exploited in order to meet the phase-matching condition. For some cases it is possible to cut or tilt the crystal in a way that the pump beam impinges onto the crystal at an angle θ eliminating the wavevector mismatch. This technique is referred to as *birefringent phase-matching*. In other cases, periodically poled crystals are used to circumvent the high precision alignment required in birefringent phase-matching, and allowing for collinear three-wave mixing. Here crystals are manufactured in such a way that every unit distance the sign of the crystal's effective nonlinear optical coefficient is flipped. This generates an additional term which compensates for the mismatch in a process called *quasi phase-matching*.

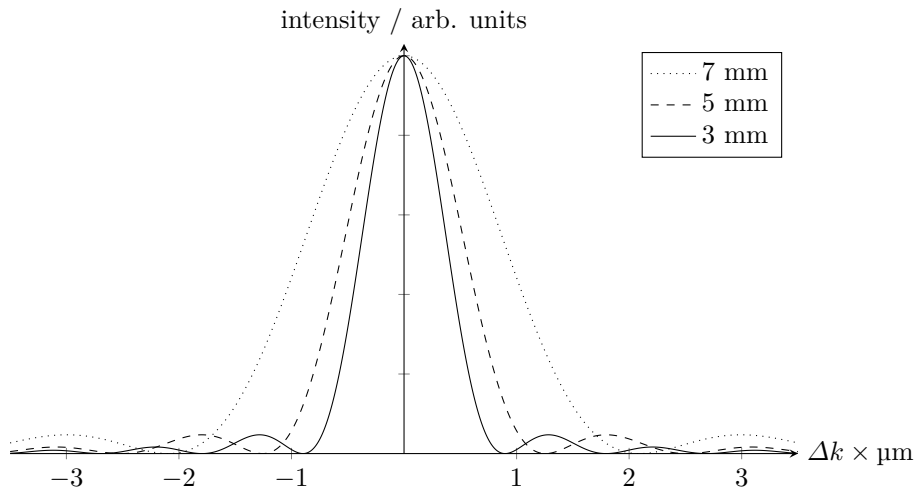


Figure 4: These curves represent crystal phase-matching tolerances depending on its length. We find the phase-matching efficiency to decrease at lower values for the wavevector mismatch $\Delta k = k_p - k_s - k_i$ for shorter crystals. Higher crystal length, on the other hand, may induce significant walk-off effects (see Section 1.4.1).

1.4.1 Birefringent Phase-Matching

Previous Sections showed that in order to maximize SPDC photon pair production according to the semi-classical approach (1.3.8), the wavevector mismatch has to be eliminated. This, however, is often difficult to achieve because the refractive index of transparent (and therefore nearly lossless) materials in the frequency range of ω_p to ω_i is often subject to normal dispersion – the refractive index increases with frequency. This poses a problem considering the wavevector mismatch can be rewritten with Equations (1.4.1) as

$$\frac{n_p\omega_p}{c} = \frac{n_s\omega_s}{c} + \frac{n_i\omega_i}{c}. \quad (1.4.2)$$

Quantities of n_p , n_s , and n_i are refractive indices of pump, signal, and idler beam, respecting their wavelength, polarization and direction. For SPDC photon pair generation where $\omega_p > \omega_s \geq \omega_i$, Equation (1.4.2) and the energy conservation cannot be satisfied simultaneously in regard of normal dispersion. Rearranging Equation (1.4.2) gives:

$$n_p - n_s = (n_i - n_s) \frac{\omega_i}{\omega_p}. \quad (1.4.3)$$

Since for positive birefringent crystals normal dispersion dictates that n_p must be higher than n_s , the left-hand side becomes positive in this particular case. On the other hand, n_s must also be greater than n_i and therefore the right-hand side contradicts the previous statement by becoming negative. Nevertheless, it is technically possible to achieve the phase-matching condition exploiting anomalous dispersion, which describes a decreasing refractive index with increasing frequency. It is however more conventional to exploit the birefringence of the crystal which enables the refractive index's polarization dependency. Except for purely cubic crystals (isotropic), all crystal systems show birefringent behavior up to some level. However, even if crystals show birefringence they are not necessarily able to compensate for normal dispersion. For phase-matchable crystals it is still necessary to select the waves' propagation direction carefully – e.g. the highest birefringent refractive index for the pump beam and so on. As for the case of a positive birefringent crystal, we choose the pump to propagate as an extraordinary beam (compare with Figure 5). Additionally, since we operate at type-II SPDC the signal and idler propagation are chosen accordingly:

$$e \rightarrow o + e \quad \text{or} \quad n_p^e \omega_p = n_s^o \omega_s + n_i^e \omega_i. \quad (1.4.4)$$

The orthogonality of signal and idler polarization does not only help with their separation but also with phase-matching, which gets substantially easier for non-degenerate SPDC i.e. $\omega_s \neq \omega_i$. The process of optimizing the refractive indices at the frequencies of pump, signal and idler, can either be done by angle or temperature tuning where in most cases it is a combination of both.

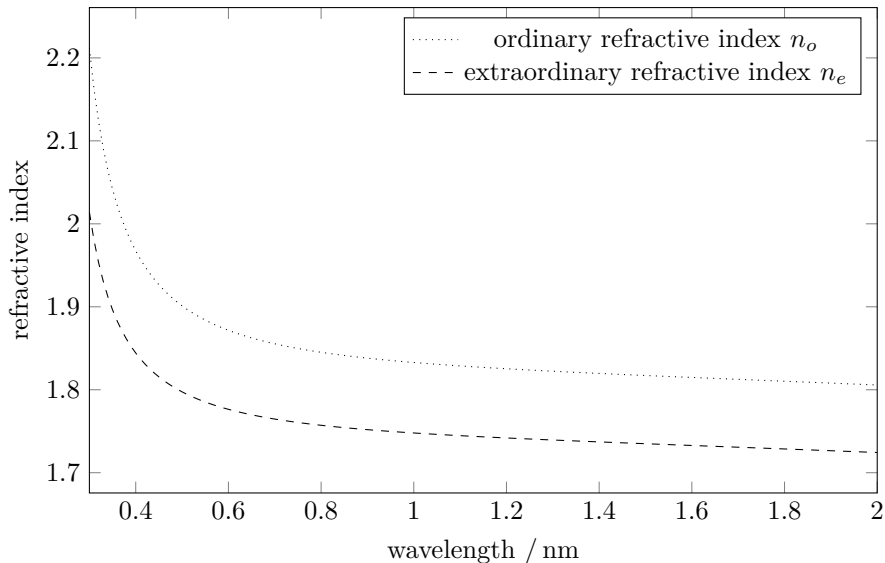


Figure 5: Typical ordinary and extraordinary refractive indices for a KTP crystal (see Appendix B).

The *angle tuning method* exploits angular dependence of the material's refractive index in order to achieve the phase-matching condition of Equation (1.4.2). It works with both uniaxial and biaxial crystal systems; calculations however, are much more complicated for biaxial systems than for uniaxial crystal systems. For uniaxial crystals, we find two distinct refractive indices such as described in Section 1.1.2. They are a result of the birefringence theory describing the angle dependent extraordinary refractive index $n_{\text{eff}}(\theta)$ (1.1.16). However, Equation (1.4.3) does not necessarily yield a solution for any birefringent crystal. In some cases the birefringence can be too weak to compensate for the dispersion in the linear refractive index. In this case the right-hand side shows values above unity which then obviously can not be matched by any θ . Unfortunately, when angle tuning, the Poynting vector $\mathbf{S} = \frac{1}{\mu_0}(\mathbf{E} \times \mathbf{B})$ and wavevector \mathbf{k} are not parallel for extraordinary rays, and consequently extraordinary and ordinary beams quickly diverge. This so called walk-off effects diminish the efficiency of the mixing process.

However, certain crystals exhibit strong *temperature-dependent birefringence* which can be used to avoid such walk-off effects. So instead of only angle-tuning the crystal for the phase-matching, the temperature dependence can be used to fine-tune the alignment.

1.4.2 Quasi Phase-Matching

Another way of increasing down-conversion efficiency is quasi phase-matching introduced by Armstrong [63]. Starting by rearranging the classical field amplitude of the DFG mixing process of Equation (1.2.17) we find

$$A_s \propto d_{\text{eff}} \sin\left(\frac{\Delta k z}{2}\right). \quad (1.4.5)$$

The electric field amplitude increases in the region of $0 < z < L_{\text{coh}}$, with the coherence length

$$L_{\text{coh}} = \pi/\Delta k, \quad (1.4.6)$$

but decreases in $L_{\text{coh}} < z < 2L_{\text{coh}}$. Due to the periodicity of the sine, we find it to be overall increasing in the interval $\{j \cdot L_{\text{coh}}, (j+1) \cdot L_{\text{coh}}\}$, with j being an even integer, and decreasing elsewhere. In order to get a continuously growing signal intensity, a proposed technique is to alternate the sign of d_{eff} as shown in Figure 6 given by

$$d_{\text{eff}}(z) = d_{\text{eff}} \cdot \text{sign}\left[\cos\left(\frac{2\pi z}{\Lambda}\right)\right], \quad (1.4.7)$$

with poling period Λ . Redoing calculation steps of Section 2.2, starting with Equation (1.2.13) with a periodical $d_{\text{eff}}(z)$ we find $I(z)$ of Equation (1.2.16) to be:

$$I(z) = \int_0^L d_{\text{eff}}(z) e^{i\Delta k z} dz. \quad (1.4.8)$$

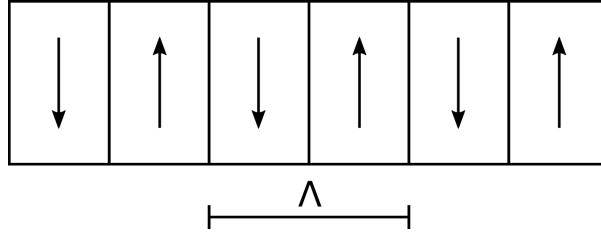


Figure 6: Schematic representation of a second-order nonlinear, periodically poled material with altered crystal orientation every half poling period.

Since $d_{\text{eff}}(z)$ is periodical we can use its Fourier series to write

$$d_{\text{eff}}(z) = d_{\text{eff}} \sum_{m=-\infty}^{\infty} G_m \exp(ik_m z), \quad (1.4.9)$$

with $G_m = (2/m\pi) \sin(m\pi/2)$, $k_m = 2\pi m/\Lambda$ and m as the Fourier order. Reinserting everything back into Equation (1.2.15) we find

$$A_s = i \frac{\omega_s}{n_s c} L A_p A_i^* \sum_{m=-\infty}^{\infty} \tilde{d}_{\text{eff}} \int_0^L \exp(i\Delta \tilde{k}_m z) dz, \quad (1.4.10)$$

while defining

$$\tilde{k}_m = \Delta k - k_m, \quad (1.4.11)$$

and

$$\tilde{d}_{\text{eff}} = d_{\text{eff}} G_m. \quad (1.4.12)$$

The nonlinear coupling coefficient \tilde{d}_{eff} here depends on the m th Fourier order. The integral can again be solved similarly to Equation (1.2.16) so that it reads

$$I_s \propto L^2 \text{sinc}^2\left(\frac{\Delta\tilde{k}_m L}{2}\right), \quad (1.4.13)$$

which shows the same shape as for the non-periodical $d_{\text{eff}}(z)$ given in Equation (1.3.8) except for a newly defined phase mismatch of

$$\Delta\tilde{k}_m = \Delta k - k_m = 0. \quad (1.4.14)$$

Using both prior definitions for phase mismatch Δk and k_m , the new phase matching condition reads

$$\Delta\tilde{k}_m = k_p - k_s - k_i - \frac{2\pi m}{\Lambda}. \quad (1.4.15)$$

Comparing it with expression of Equation (1.4.14), it becomes obvious that the relation for the poling period follows

$$\Lambda = \frac{2\pi}{\Delta k} m. \quad (1.4.16)$$

Since \tilde{d}_{eff} tends to decrease at higher orders of the Fourier coefficients m , it is preferable to always achieve quasi-phase matching in a first order interaction ($m = 1$). As a consequence of the quasi phase-matching, the signal field intensity increases consistently because the additional term in (1.4.15) compensates for any phase mismatch. The case of quasi phase-matching is depicted against perfect and non-phase-matching in Figure 7 (left).

In order to operate a single-photon source with a ppKTP crystal as the core element of an heralded single-photon source, it is necessary to design its poling period according to the quantum memory's acceptance requirements. As the crystal's refractive indices may also contain a temperature dependency, described by the Sellmeier equations, it is necessary to include a temperature dependence in the quasi phase-matching condition of Equation (1.4.15). By solving it together with the energy conservation, we find solutions for corresponding signal and idler wavelength similar to what is depicted in Figure 7 (right). Since we aim to operate the source in a temperature range from room temperature up to 50 °C we require a poling period $\Lambda = 10.1 \mu\text{m}$.

1.5 Influence of Cavity Mode Structure on OPO Tuning

Down-conversion photon pair sources are by nature broadband sources and exhibit bandwidth up to a couple of THz [64]. In order to contain the photon's bandwidth within a MHz regime it is necessary to design an OPO resonant for signal and idler waves. Its length defines the separation, or *free spectral range* (FSR), of the transmitting modes given by

$$\Delta\nu = \frac{c}{2nL} \quad \text{or} \quad \Delta\omega_c = \frac{\pi c}{nL}, \quad (1.5.1)$$

where n is the refractive index behaving according to the Sellmeier equations (1.1.15). In order to reduce the resonances' full width at half maximum (FWHM) to match the quantum memory it is necessary to establish the cavity's finesse

$$\mathcal{F} = \frac{\pi}{2\arcsin\left(\frac{1-\sqrt{\rho}}{2\sqrt[3]{\rho}}\right)}, \quad (1.5.2)$$

which purely depends on the fraction ρ of the power left after one cavity round-trip. The FSR divided by the finesse defines the transmission peaks' FWHM. By increasing the mirrors reflectivities we can consequently reduce the resonance's bandwidth to match them with the quantum memory. For the case of the doubly resonant OPO, meaning both mirrors show highly reflective dielectric coatings for signal and idler frequencies, two comb structures build up simultaneously each depending on the

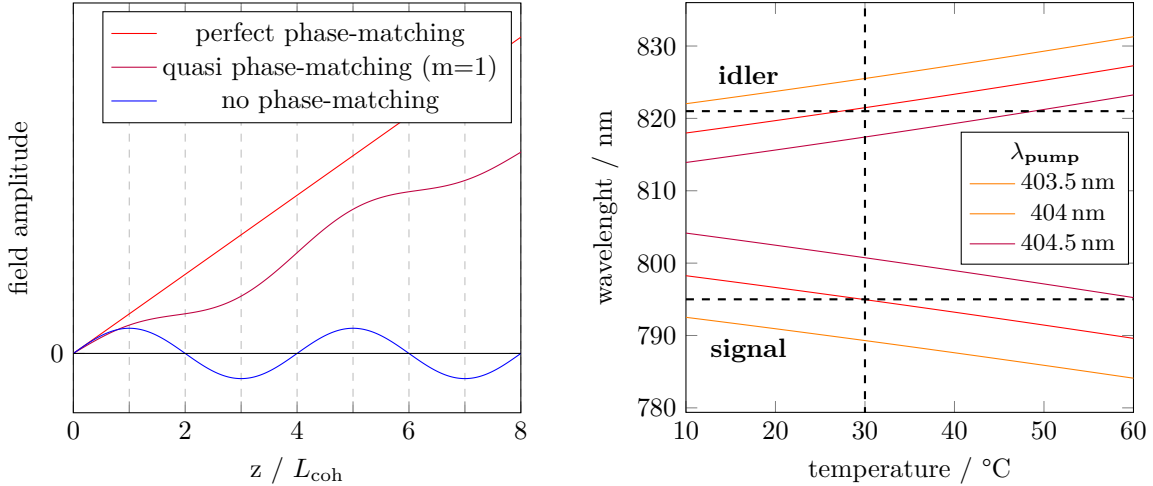


Figure 7: Comparison of signal field amplitudes in the crystal for three cases; phase-matched, non-phase-matched and quasi phase-matched (left). The solutions for signal and idler wavelengths from energy conservation and quasi phase-matching condition for temperature depended refractive indices given in Appendix B (right). In order to satisfy both conditions a target wavelength of 795 nm and a pump wavelength between 403.5 nm and 404.5 nm, we expect that the crystal needs to be operated at 30 °C if we choose $\Lambda = 10.1\mu\text{m}$.

other due to energy conservation. However, due to the frequency dependence of the refractive indices, we find frequency combs of different separations imposed by Equation (1.5.1). The oscillating mode is then strongly favored under phase-matching conditions proposed in chapter 1.4. Consequently, the oscillating mode might be far from either closest modes of the idler and signal comb (compare with Figure 8). This is also the reason for doubly resonant OPOs not to tune smoothly. The resulting effective mode structure is a product of the mode structures given by signal and idler waves as depicted in Figure 9

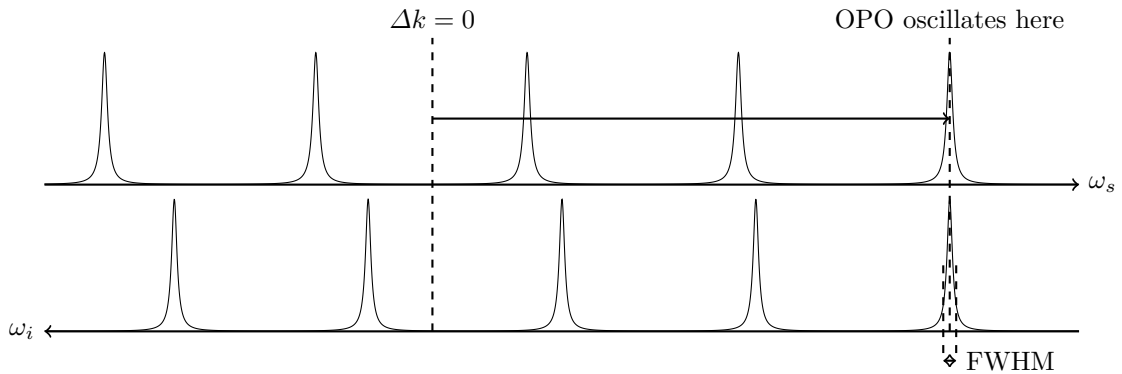


Figure 8: Representation of two OPO resonant structures such as in a doubly resonant OPO. Due to opposite directions of idler and signal axes, every point on the axis obeys energy conservation. Oscillation only occurs at the point closest to $\Delta k = 0$ at which the double-resonance condition is satisfied.

Since both signal and idler photons propagate within the resonator it is necessary to introduce the energy mismatch

$$\Delta\omega = \omega_p - \omega_s^{(m)} - \omega_i^{(m)}, \quad (1.5.3)$$

where $\omega_s^{(m)}$ and $\omega_i^{(m)}$ are the signal and idler crystal mode frequencies accepted by the resonator geometry, respectively. Clearly, signal and idler frequencies are still underlying the energy conservation introduced in Section 1.4 and therefore $\Delta\omega \approx 0$. However, considering these modes exhibit a non-zero linewidth, we find renewed boundary conditions for pair production:

$$\Delta\omega \lesssim \text{FWHM}, \quad (1.5.4)$$

with FWHM as the spectral width of a typical cavity mode. In order to calculate the spectral separation between two clusters as illustrated in Figure 9 we need to start by estimating the frequency difference between a signal and an idler FSR:

$$\delta(\Delta\omega) = \frac{\pi c}{L} \left(\frac{n_i - n_s}{n_s \cdot n_i} \right). \quad (1.5.5)$$

Subsequently, we try to find the spectral distance between the points of phase-matching $\Delta k = 0$ and $\Delta\omega = 0$ as depicted in Figure 8. It is very unlikely to find both conditions satisfied simultaneously. In fact, the spectral difference between these two points can become very large for small differences in signal and idler refractive indices. However, this spectral difference is limited since after a certain number of FSRs, another, more suitable cluster for satisfying the conditions appears, provided that the phase-matching bandwidth is large enough. This effect prevents the energy mismatch from exceeding half an FSR in both directions. Summing up the maximum spectral difference for both direction gives a total energy mismatch of one FSR. Consequently, assuming the cavity FSR for signal and idler to be similar ($n_s \approx n_i$), the number of modes separating two clusters is

$$N = \frac{\text{FSR}}{\delta(\Delta\omega)}. \quad (1.5.6)$$

Multiplied with the typical cavity FSR yields the spectral cluster separation according to [41]

$$\Delta\omega_{\text{cluster}} = \text{FSR} \cdot N \approx \frac{\pi c}{L} \cdot \frac{1}{n_s - n_i}. \quad (1.5.7)$$

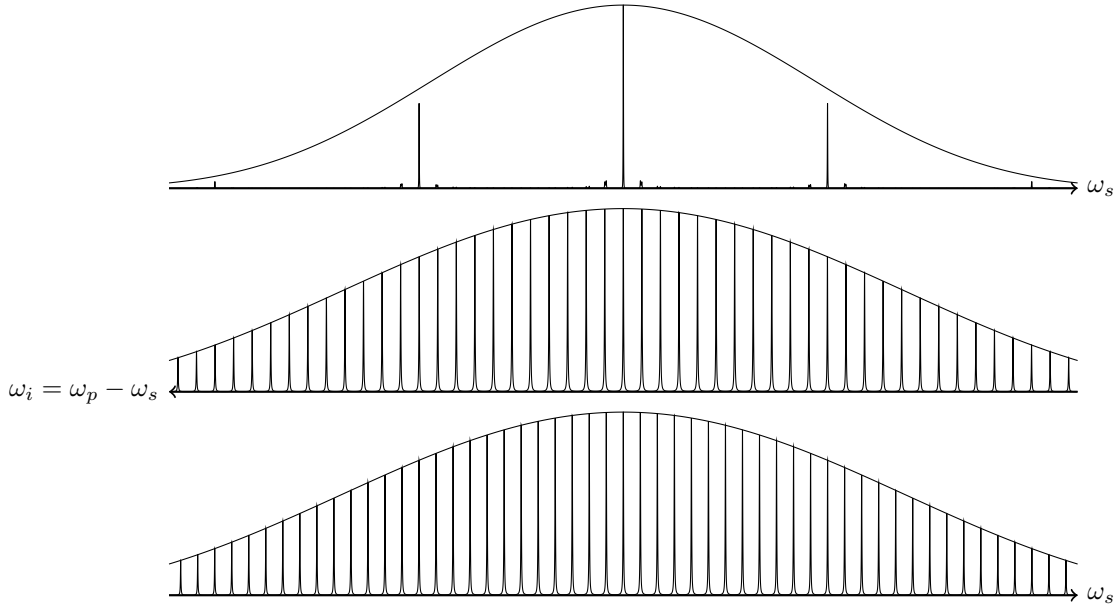


Figure 9: Frequency combs of signal (bottom) and idler (center) and their product (top). It is displayed for the case of a central frequency satisfying both $\Delta k = 0$ and $\Delta\omega = 0$. The height of the peaks are limited by the phase-matching envelope.

1.6 Correlation Functions

In order to quantify the performance of light sources, some mathematical tools together with a certain quantum-mechanical know-how are needed. In the 1960s, Glauber and others showed the construction of quantum correlation functions by using the atom-field interaction Hamiltonian given by

$$\mathcal{H}^{(I)} = -\mathbf{d} \cdot \mathbf{E}(\mathbf{r}, t), \quad (1.6.1)$$

with \mathbf{d} being the dipole operator. The first and second-order correlation functions with their normalized counterparts are given by [65]:

$$G^{(1)}(\mathbf{r}_1, t_1, \mathbf{r}_2, t_2) = \langle \psi | E^-(\mathbf{r}_1, t_1) E^+(\mathbf{r}_2, t_2) | \psi \rangle, \quad (1.6.2a)$$

$$g^{(1)}(\mathbf{r}_1, t_1, \mathbf{r}_2, t_2) = \frac{G^{(1)}(\mathbf{r}_1, t_1, \mathbf{r}_2, t_2)}{\sqrt{G^{(1)}(\mathbf{r}_1, t_1, \mathbf{r}_1, t_1) \cdot G^{(1)}(\mathbf{r}_2, t_2, \mathbf{r}_2, t_2)}}, \quad (1.6.2b)$$

$$G^{(2)}(\mathbf{r}_1, t_1, \mathbf{r}_2, t_2) = \langle \psi | E^-(\mathbf{r}_1, t_1) E^-(\mathbf{r}_2, t_2) E^+(\mathbf{r}_2, t_2) E^+(\mathbf{r}_1, t_1) | \psi \rangle, \quad (1.6.2c)$$

$$g^{(2)}(\mathbf{r}_1, t_1, \mathbf{r}_2, t_2) = \frac{G^{(2)}(\mathbf{r}_1, t_1, \mathbf{r}_2, t_2)}{G^{(1)}(\mathbf{r}_1, t_1, \mathbf{r}_1, t_1) \cdot G^{(1)}(\mathbf{r}_2, t_2, \mathbf{r}_2, t_2)}, \quad (1.6.2d)$$

with electric field operators $E^{+/-}$ according to definition of Equation (1.3.1) for positive and negative frequency parts respectively. In order to account for important two photon statistics of the photon pair source we need to consider correlation functions at least up to second-order. These can be used to examine whether the extracted quantum states meet the requirements imposed by the quantum memory.

To examine the photon statistics of our heralded single-photon source, we initially measure the autocorrelation functions. We expect signal and idler arm to show individually a thermal statistics resulting in bunching peak at zero time delay τ between detector 1 and 2 [66, 67]. In fact, according to [41] the autocorrelation reaches a value of

$$g_{x,x}^{(2)}(0) = 1 + 1/n, \quad (1.6.3)$$

where n is the number of modes and x stands for either signal or idler. This is due to the inherent thermal photon statistics of each individual arm for signal and idler photons [68]. In practice, we expect the photon statistics to go as high as 2 for a single mode. However, this applies only for photon generation probabilities per coherence time p well below unity, or pump powers far below threshold. By restraining the pump power we can strongly suppress higher order N photon pair number states whose success probability scales with $P \propto p^N$. Furthermore, if the source's crystal does not support ultra narrow modes, one needs to take into account the photons bandwidth. The ideal shape of the photon autocorrelation is given by [69] as

$$g^{(2)}(\tau) = 1 + \exp(-2|\tau|/\tau_0). \quad (1.6.4)$$

where the coherence time $\tau_0 = 1/(2\pi\text{FWHM})$ for a Lorentzian line shape, such as for the emerging photon pairs of the source.

Conditioning the the signal autocorrelation upon an idler detection event retrieves additional statistics of the single-photon character of the source. We expect it to increase with higher pump power which accounts for higher photon generation rates. However, as implied earlier in this Subsection, by increasing the pump power, the photon generation probability per coherence time p increases and consequently increases the probability of higher order photon pair generation events. These higher order events manipulate the statistics in a way that at high powers we cannot be certain to have generated only a single photon pair. The higher order photon states contaminate the single-photon character of the source so that it becomes unusable for any storage applications.

Finally, to ensure that the source emits explicitly photon pairs it is advised to check the crosscorrelation between signal and idler photons. We expect to see that

$$g^{(2)}(0) \gg 2, \quad (1.6.5)$$

which implies super-thermal bunching according to [68] and thus indicates signal-idler pair generation.

2 Doubly Resonant Monolithic OPO with Double Pass Pump Scheme

In order to set up a compatible single-photon source to operate the warm rubidium vapor quantum memory proposed by Wolters et al. [48] with, we need to design our source according to the requirements imposed by the memory’s specifications. First, the wavelength of the single photons must match the memory’s target wavelength which is here given by the D₁ line of ⁸⁷Rb atoms at $\lambda = 795$ nm [70] with a small detuning in the order of 1-2 GHz. Second, the bandwidth of the photons has to be matched to the accepting bandwidth of the memory. Fortunately, the rubidium memory shows a relative wide acceptance bandwidth, which allows for pairing with a narrow bandwidth photon-source [51]. In order to meet the memory’s bandwidth requirements we need to generate photons with a spectral width between 100 MHz and 1 GHz. Third, high extraction or heralding efficiencies are necessary to surpass readout noise. In order to achieve a unity readout signal-to-noise ratio, heralding efficiencies of 25% and higher are needed. Finally, it is required to exceed herald rates of 50 000 counts/s to be three orders of magnitude higher than the dark counts.

There have been a number of different ideas to set up a single-photon source with SPDC [71, 72] but we decided to iterate a triply resonant monolithic OPO with multi-pass pump scheme design [51] which has been successfully paired with our memory [50]. As a central element, the source uses a ppKTP crystal with highly reflective dielectric coatings on both facets for signal, idler, and photons. This design enables pump light recycling but accelerates gray-tracking in the crystal which decreases its performance significantly. In order to slow down gray-tracking we implement a double-pass pump scheme by omitting one high reflective dielectric coating for 404 nm. In return, we lose the ability to lock the pump laser onto the laser transmission modes of the crystal. It is therefore necessary to install an external cavity to lock the pump laser. For long time measurements our aim is to reduce the frequency drifts of the cavity to 10 MHz/h in a time window of 10 hours.

2.1 Setup

Similarly to the previous version of the SPDC heralded single-photon source, we use a ppKTP crystal as a central element with a curved and a planar facet to form a stable hemispherical cavity. In contrast to the prior version, we omit high reflective dielectric coatings for the grating stabilized 404 nm diode laser on the curved facet. The idea is that the pump light penetrates into the curved facet and down-converts into a signal ($\lambda_s = 795$ nm) and idler ($\lambda_i = 822$ nm) photon pair according to the phase matching theory of Section 1.4. The crystal’s reflective coatings for signal and idler photons are chosen so that the emergence of photon pairs is strongly biased towards the planar facet. To the right of the crystal in Figure 10, a high transmission longpass filter (*AHF Analysentechnik*) is installed to reflect the transmitted pump light so that it does not contaminate the signal. Subsequently, a $\lambda/2$ -waveplate rotates the polarization of signal and idler photons which are initially polarized vertically and horizontally respectively. This is necessary to exploit the polarizing beamsplitter’s significantly better performance in transmission for signal photons which results in a better heralding efficiency.

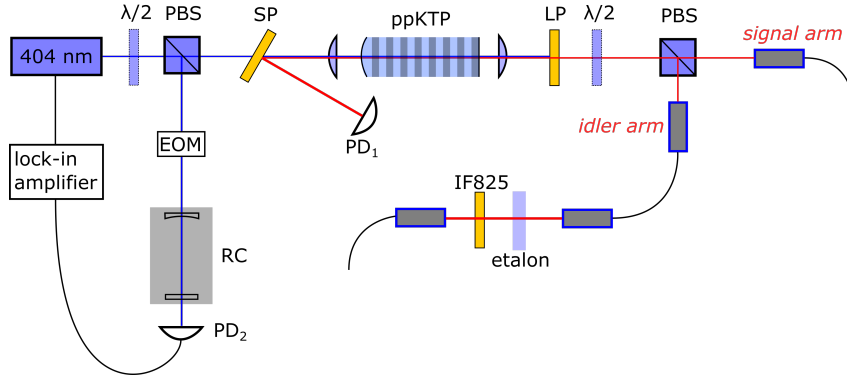


Figure 10: Experimental setup used to pump the OPO and to collect SPDC photon pairs in optical fibers. The crystal is coated so that the photon pairs are strongly biased to exit the planar facet. The longpass (LP) reflects residual pump light and the $\lambda/2$ -waveplate rotates the idler and signal polarization. By doing so we can exploit that polarizing beamsplitter (PBS) exhibit better performances in transmission than reflection. The filter stage for the idler photons includes an etalon and an interference filter (IF) to spectrally select a single emission mode. SP: shortpass filter. PD: photodiode. RC: reference cavity. EOM: electro-optical modulator.

In order to allow any characterization measurements or to utilize the heralded single photons for storage experiments, we directly couple signal photons into an anti-reflection coated, single mode, polarization maintaining fiber. The idler photons, on the other hand, are filtered with a etalon and an interference filter to a single emission mode of the cluster. The temperature controlled etalon shows, with a thickness of 1.00(5) mm, an FSR of 102(5) GHz and an FWHM of 1.8(1) GHz. Its transmission maximum is at 93%. The interference filter depicted in Figure 10 is angle-tuneable and transmits $> 90\%$ with a FWHM=0.57(5) nm at 822 nm [48].

Since we omit the reflective coating for the 404nm laser on the planar facet, we not only limit the number of round-trips of the pump light but we lose at the same time a reference cavity for the laser. To compensate for the missing lock, we installed a $\lambda/2$ -waveplate in a rotational mount in combination with a polarizing beam splitter right after the pump laser which reflects less than 10% to a reference cavity. The cavity is a hemispherical design, equipped with a 10 cm cylindrical Zerodur spacer which forms a passively stable cavity. Since the cavity does not provide any degrees of freedom, we need a broadband electro-optical modulator (EOM, from *Qubig*) to generate sidebands to overlap with the target frequency to lock on. The lock-in amplifier then generates an error signal which feeds the PID controller of the laser.

2.1.1 ppKTP Crystal

The core element of the heralded single-photon source is a ppKTP crystal (grown by *Raicol Crystals*, polished by *Photon LaserOptik*, and coated by *Lens-Optics* and *Laseroptic* for the planar and curved respectively) with dimensions of $1 \times 2 \times 5$ mm³ (Figure 11). It is polished to form a hemispherical Fabry-Pérot resonator for both the signal and idler wavelengths, where the curved facet exhibits a radius of curvature of 10 mm. Specifically, the high reflective dielectric coatings for the planar (curved) facet are designed as $R_{s/i}^p = 91.5\%$ ($R_{s/i}^c = 99.9\%$) for the signal and idler frequencies, and $R_p^p = 99\%$ ($R_p^c < 1\%$) for the pump frequency. The dielectric coatings are used for bandwidth control of the photons, specifically of the signal photons, to ensure compatibility with the memory. The coatings are carefully chosen so that we find a finesse of $\mathcal{F} = 69.9$ with Equation 1.5.2. The fraction of power left after one round-trip is $\rho = 99.9\% \times 91.5\% = 91.4\%$. Finesse expressions of Equation (1.5.2) and

$$\mathcal{F} = \frac{\text{FSR}}{\text{FWHM}}, \quad (2.1.1)$$

together with the expression for the FSR governed with Equation (1.5.1), we find the theoretical values for the signal (idler) FSR= 17.1 (16.3) GHz and the signal FWHM= 244 MHz.

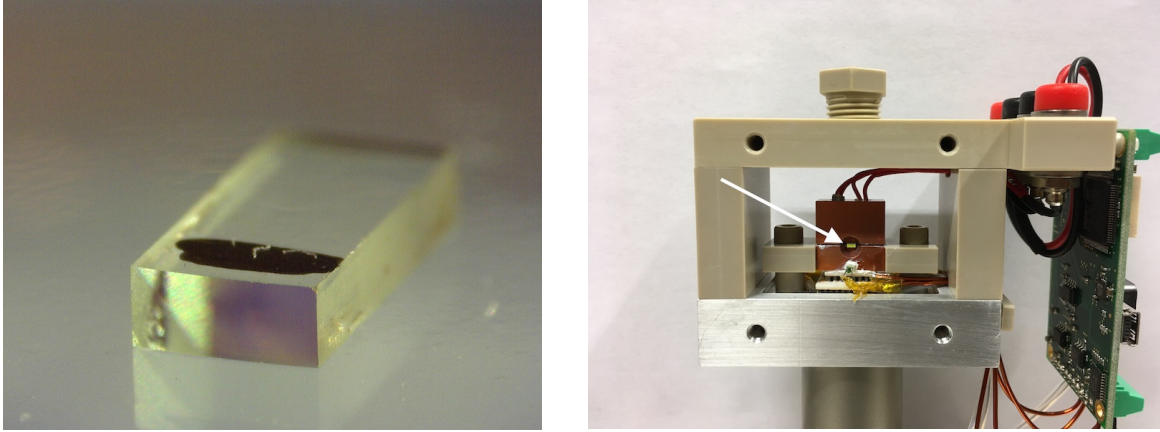


Figure 11: The ppKTP crystal has a curved (black mark) and a flat facet (left). It is clamped between two copper plates placed in a PEEK housing (right, stripped for demonstration) with a peltier element underneath, thermalizing the crystal. The peltier element generates a temperature difference between the object (copper plates and the crystal above) and the heat sink (aluminum plate below). The temperature is controlled with two temperature probes placed at either plate connected to the printed circuit board attached to the right side of the housing. The PEEK screw on top and the two heating rods connecting the two copper plates are currently redundant.

The crystal is designed with a poling period $\Lambda = 10.1 \mu\text{m}$, which is used for the down-conversion to obey the type-II quasi phase-matching conditions of Section 1.4.2. Using the temperature dependent refractive indices of Appendix B, we can estimate at what temperature the conditions are satisfied. By simply inserting them into the quasi phase-matching conditions, Equations (1.2.2) and (1.4.14), we find results displayed in Figure 7. In fact, we find for a pump wavelength of 404 nm a crystal temperature of 30°C which coincides with the design temperature, introduced in chapter 1.4.2. Pump wavelength and crystal temperature are the most important parameters to work with because they greatly influence the phase-matching conditions. As a side-effect, they also influence the crystal's dimensions, most importantly the crystal length. These length variations change the cavity FSR and the crystal's poling period, imposing a new set of phase-matching conditions. Since it becomes difficult to generate a model accounting for all factors, it is advisable to fine-tune the working parameters experimentally.

2.1.2 Sideband Offset Lock

The 404 nm diode laser is not locked and therefore exhibits significant frequency shifts up to 100 MHz/h in normal working conditions. In order to manage long term measurements up to 10 hours while keeping the shifts rate well below 10 MHz/h, we require a laser lock. We opted for an external cavity with hemispherical design with a length of 100 mm, embedded in a thermally stabilized environment and with the option of being evacuated. The hemispherical resonator design is proven to support large mode size differences and is therefore implemented as a fail-safe option [73]. This cavity design is therefore optimal to form a passively stable cavity. In combination with an EOM, this is a design proven to be suitable to support a lock-in amplifier sideband offset lock which enables tuneability due to the sideband modulation. The cavity spacer is a low thermal expansion Zerodur cylinder equipped with a spherical and a planar mirror showing reflectivities of 92.5% and 99% for signal/idler and pump wavelength respectively.

2.2 Difference Frequency Generation

Given by its spontaneous nature and the pump operation regime far below threshold, SPDC single photons are not so numerous to enable any coarse adjustment. In order to perform initial coarse adjustments, we use laser light from a calibrated 795 nm diode laser (from now on referred to as seed laser) to mimic both signal and idler photons. For this purpose it is coupled backwards into the signal arm (see with Figure 10) and mode-matched onto the crystal. To use the seed light for filter stage adjustments, a $\lambda/4$ -waveplate is placed between the longpass and the $\lambda/2$ -waveplate. The $\lambda/4$ -waveplate changes the light's polarization on the way to the crystal and after the reflection from the crystal surface and therefore rotating the polarization by 90° . Instead of transmitting through the PBS it now gets reflected in the idler

arm where it can be used to tune the filter stage. However, to fine-tune spectrally sensitive elements, such as filters and couplings, we need photons at exactly the idler wavelength at around 822 nm. These photons can be generated by stimulating, or seeding, the pumped crystal following the DFG theory and therefore generating much higher pair rates. The emerging stimulated photon pairs behave accordingly to the energy diagram shown in Figure 2 and show identical properties to the SPDC signal and idler photons. The high photon rates not only allow for coarse adjustments, but also to effortlessly operate spectral scans to resolve emission cluster in relatively a narrow spectral range compared to a spectrometer. Furthermore, it promotes the tuneability of the source by enabling easy switching from one emission peak to another.

Another advantage of the DFG operation over SPDC is that it enables optimization of the filter stage placed in the idler arm (see Figure 10). DFG allows us to optimize the temperature of the etalon and the angle of the interference filter for maximal transmission of the target frequency. Overall we accomplished a peak transmission efficiency for the total filter stage of about 87%.

2.3 Crystal Characterization Measurements

The coatings provide a resonator cavity for signal and idler wavelengths within the crystal. We probe the crystal with the 795 nm seed laser in order to observe a transmission mode spectrum on PD₁. The spectrum, depicted in Figure 12, shows an FSR of 17.5(2) GHz which agrees well with the theoretical value of 17.1 GHz. The transmission peaks exhibit a FWHM of 373(1) MHz which converts together by way of Equation (2.1.1) to an experimental cavity finesse of 32(2).

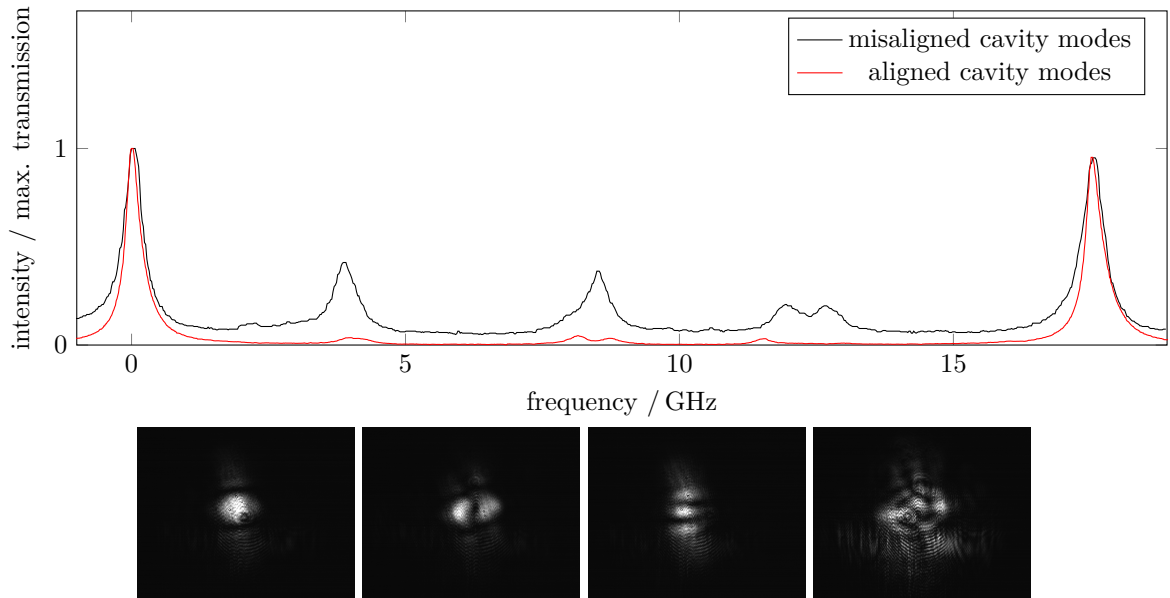


Figure 12: These are the modes to be found for a slight misalignment of the cavity (black) and for an optimally aligned cavity (red) observed with PD₁ in Figure 10. The snapshots below are obtained using a camera to analyse individual modes from left to right in order of increasing frequency. The mode pictured on the far left corresponds to the fundamental mode and should be optimized in order to proceed.

After characterizing the mode spectrum of the crystal with the seed laser, we planed to seed the pumped crystal to operate DFG in order to verify the alignment of the pump laser and the working parameters – crystal temperature T_{KTP} and pump wavelength λ_{pump} . The crystal temperature and pump wave for which we created our crystal for are 30 °C and $\lambda_{\text{pump}} = 404$ nm (compare with Figure 7, right). However, DFG can only be generated if the signal target frequency coincides with one of the transmission modes of the crystal. Considering that a shift of the cavity spectrum of the crystal by one FSR occurs for a temperature change of around 3 °C, we found two temperature settings adjacent to 30 °C: 29.3 °C and

32.3 °C, governed by probing the crystal with only the seed laser. The pump wavelength, however, is not tied to the any transmission conditions of the cavity and can theoretically be tuned continuously. By testing both temperature settings with the pump laser detuned around the target frequency, we could generate an initial DFG signal.

In a subsequent step, we tried to verify the best possible working parameters in proximity of the design parameters. By doing so, we switched to SPDC operation for which we could use a single-photon spectrometer with a deep cooled scientific CCD camera with ultra-low-noise electronics (from *Princeton Instruments*, Figure 13 left). Instead of being limited by the scan range of the seed laser, the spectrometer resolves over multiple nanometers. By playing around with the working parameters, we could verify the behavior of the emission peaks. Increasing the crystal temperature within a small range, as depicted in Figure 13 (left), shifts the emission cluster peaks towards longer wavelengths. This is on the one hand caused through temperature-dependent refractive indices and on the other due to changes in the crystal length. Wavelength changes, however, affect the emission peaks in less predictable way. In theory, wavelength shifts do not move the transmission peaks since they only depend on the crystal temperature but not on the pump wavelength. So as we change the pump wavelength, we expect the heights of the peaks to vary according to the energy conservation. In practice however, we experience shifts in the transmission peaks which are induced by temperature changes introduced by the pump laser as depicted in 13 (right). These are apparent for large pump detunings as the pump laser may not tune smoothly. Additionally, the crystal's absorption does not necessarily have to be the same for all wavelength in this range.

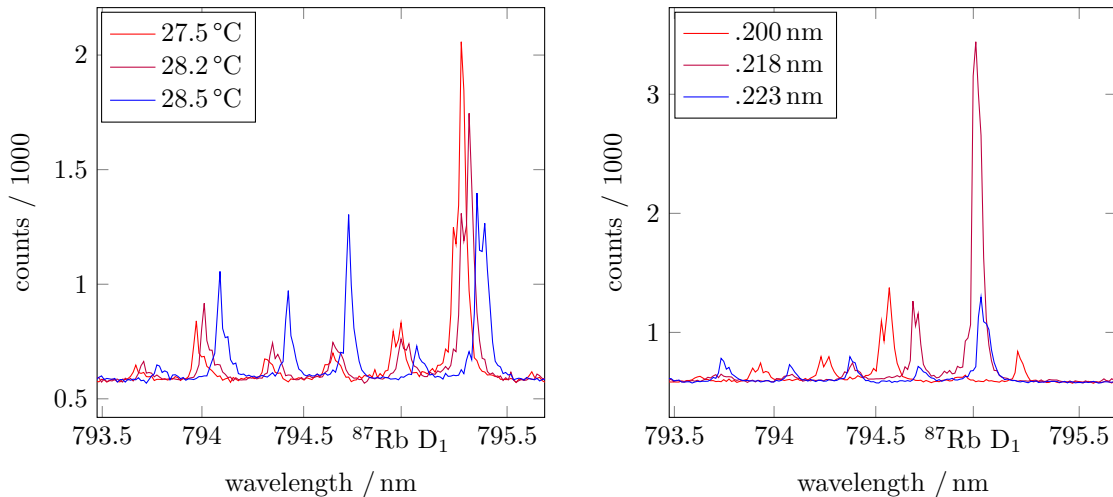


Figure 13: Effects of changes in the crystal temperature on the emission spectrum of the crystal measured with a spectrometer over an integration time of 15 seconds at a pump power of 3 mW and at a pump wavelength $\lambda_{\text{pump}} = 404.218$ nm (left). By increasing the temperature the peaks shift to longer wavelengths. For a temperature change of 3 °C the spectrum shifts one cavity FSR. The height of the peaks is determined by the phase matching envelope. Changes in the pump frequency are harder to examine (right). These spectra are acquired for a crystal temperature $T_{\text{KTP}} = 29.3$ °C and pump wavelengths around 404.2 nm. In theory, they should shift the phase-matching envelope while the emission peaks remain at their initial position dictated by the transmission spectrum of the crystal. Pump light absorption, however, heats the crystal and complicates simulations. The differences between 404.2 nm and the other measurements may be due to different pump laser performance or the difference in absorption for these wavelength.

In conclusion, in order to find optimal working parameters for SPDC operation it is required to fine-tune both parameters since they are intertwined. In the end, once the three conditions for energy conservation, phase-matching, and crystal transmission are fulfilled by the two degrees of freedom, we find a strongly pronounced emission peak. In fact, this can be done for any particular target frequency in the vicinity of 795 nm and ensures convenient tuneability of our source. For our target wavelength, situated at the ^{87}Rb D₁ line, we found parameters $T_{\text{KTP}} = 29.3$ °C and $\lambda_{\text{pump}} = 404.218$ nm. The corresponding

emission spectrum is shown in Figure 14. Overlaying the spectrum with its corresponding idler spectrum and seed laser tuned to the target frequency ensures that the spectrum is not contaminated and that miscalibrations of the spectrometer are excluded. Additionally, we scanned the strongest emission peak with the seed laser to resolve the adjacent peaks as depicted in Figure 14 (right). By doing so, we found that the central peak contributes to more than 75% the total emission of the cluster.

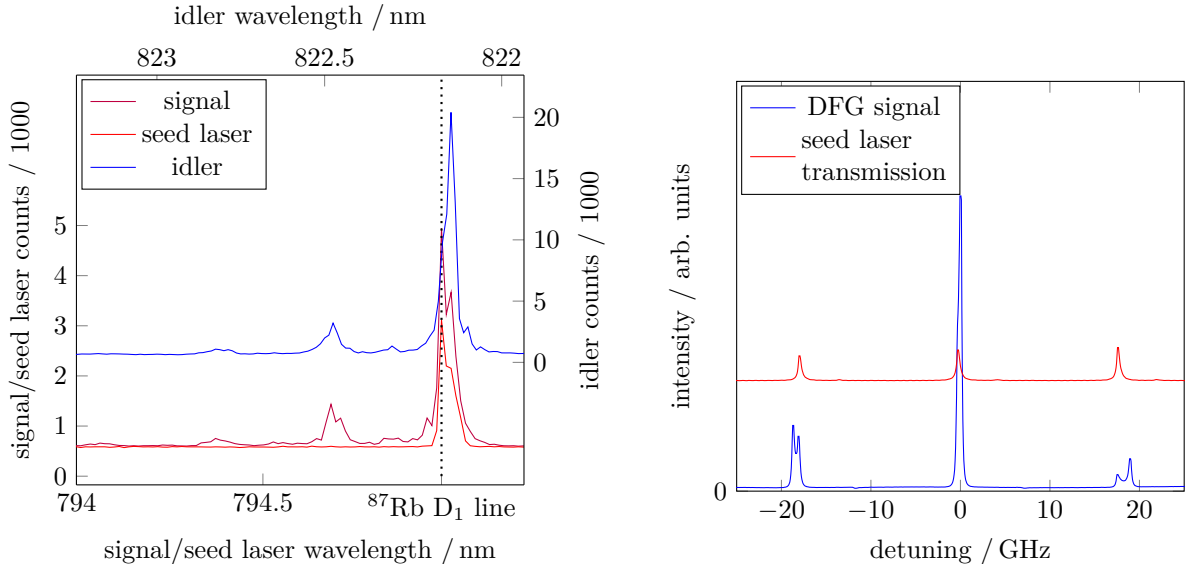


Figure 14: The SPDC spectrum shows a highly pronounced peak which is overlaid with its corresponding idler spectrum around 822 nm for an integration time of 15 s and a pump power of 3 mW (right). In order to check the degree of overlap of signal photons of the down-conversion crystal with the target frequency, we used the seed laser tuned to the transition frequency as a reference. We found optimal working parameters for a strongest pronounced cluster emission peak to be $T_{KTP} = 29.3^\circ\text{C}$ and $\lambda_{\text{pump}} = 404.218\text{ nm}$. This strong emission peak can be better resolved in the DFG operation as a function of the seed laser detuning (right). For this particular spectrum we scanned over 50 GHz around the target frequency and found that smaller adjacent double peaks of the strongly pronounced cluster are separated by around one signal and idler FSR, respectively, from the central peak.

2.4 Reference Cavity Characterization Measurements

In a first step, we coupled a 795 nm laser equipped with a Doppler-free saturation spectroscopy of a rubidium vapor cell into the cavity. The atomic spectroscopy serves as an absolute frequency reference for the cavity modes and therefore helps to examine if there are any higher order modes spuriously coupled into the cavity. In our case, we found cavity modes separated with 1.45(3) GHz which coincides with the theoretical value governed by Equation (1.5.1). Another indicator of a well coupled cavity is the FWHM of the cavity modes. Comparing the expression for the finesse of the cavity of Equation (1.5.2) to the experimental expression of Equation (2.1.1), we can estimate if more careful coupling is required. In our case, we found a considerable mismatch of theoretical and measured values. This mismatch, however, does not originate in careless coupling but is due to the cavity geometry which will be discussed in the Section 3.

In a subsequent step, we need to make sure that the reference cavity remains stable to meet the requirement to remain below 10 MHz/hour shifts over long time periods. For testing, we again need the 795 nm laser referenced with the Doppler-free saturation spectroscopy. In order to perform the long time stability measurement, we recorded both the cavity spectrum and the atom reference spectrum simultaneously every half hour over a period of ten hours. The analysis, however, is a bit more sophisticated than for previous cavity spectrum scans. In order to adopt an absolute frequency axis and to compensate for the nonuniform scan speed of the laser, we developed a tool which uses all the resolved Rubidium transition peaks as frequency indicators. We found that a second-order polynomial fit accounts sufficiently for the

nonlinearity. The procedure together with the adjusted transmission mode spectrum is illustrated in Figure 15.

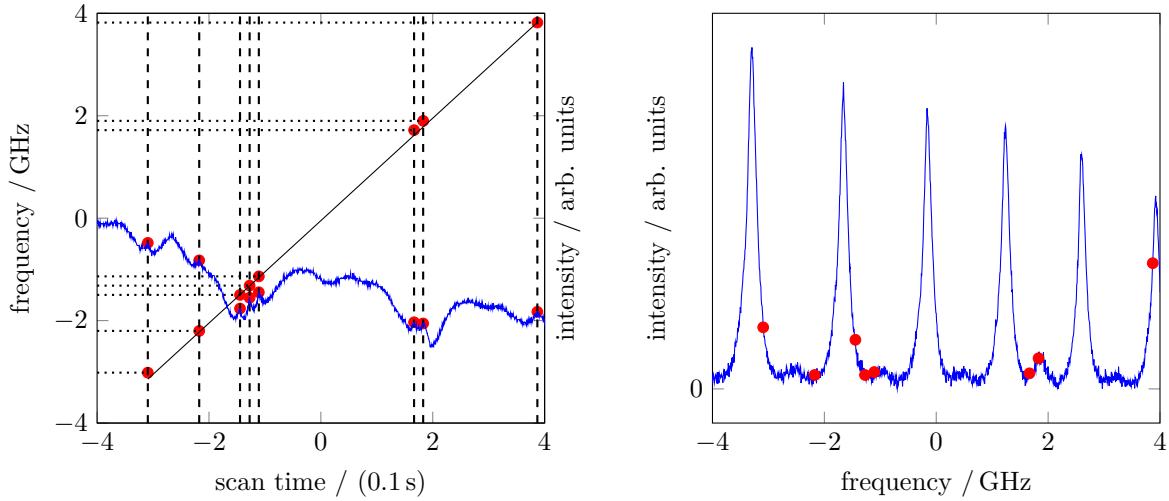


Figure 15: The procedure to convert a time axis of the scan into a frequency axis while accounting for nonlinearities in the scan speed. Since both the Doppler-free saturation spectroscopy of ^{87}Rb (left) and cavity transmission peaks (right) are recorded simultaneously, they exhibit both the same scan nonlinearity. However, since the atomic spectrum is an absolute reference and frequency differences between transmission peaks (marked in red) are well known, we can overlay the spectrum with a frequency axis by using a second-order polynomial fit (left, in black).

While repeating this procedure every 30 minutes over a time period of 10 hours, we could assess that the frequency shifts remain below 10 MHz/h, except for the initial 3 hours. However, we did not yet initiate evacuating the cavity. In fact, the cavity remained open during this time period and was therefore exposed to the unstable environment of the lab during working hours during the initial 3 hours.

In order to lock the laser frequency onto the reference cavity signal we need to find a way to generate a peak at the target pump frequency. Since the cavity length is fixed and stable by design, one way of peak generation is the modulation of sidebands using an EOM. Theoretically, the sidebands take the form [54]

$$\begin{aligned}
 E_{\text{mod}} &= E_0 e^{i(\omega t + \beta \cos(\Omega t))} \\
 &\approx E_0 e^{i\omega t} \left[1 + \frac{i\beta}{2} \left(e^{i\Omega t} + e^{-i\Omega t} \right) \right] \\
 &= a_0 e^{i\omega t} + a_- e^{i\Omega - t} + a_+ e^{i\Omega + t}
 \end{aligned} \tag{2.4.1}$$

where β and Ω are the modulation depth and modulation frequency respectively. The coefficients a_0 , a_- , and a_+ describe the amplitudes of the central peak and the sidebands and depend greatly on the modulation depth. Additionally, in the second step of the calculation, we used the cosine identity $\cos(x) = 1/2(e^{ix} + e^{-ix})$. The modulation frequency, allowing for sideband modulation tuning, ranges for our device from 750 MHz to 1.5 GHz. Comparing this to the cavity FSR of 1.45 GHz, we find that there is always one possible sideband to lock onto (see Figure 16, right). In order to generate an error signal, the lock-in amplifier demodulates the kHz modulation, initially imposed on the light by the laser, and feeds it to the PID controller. The PID controller then processes the signal and enables a top-of-fringe lock.

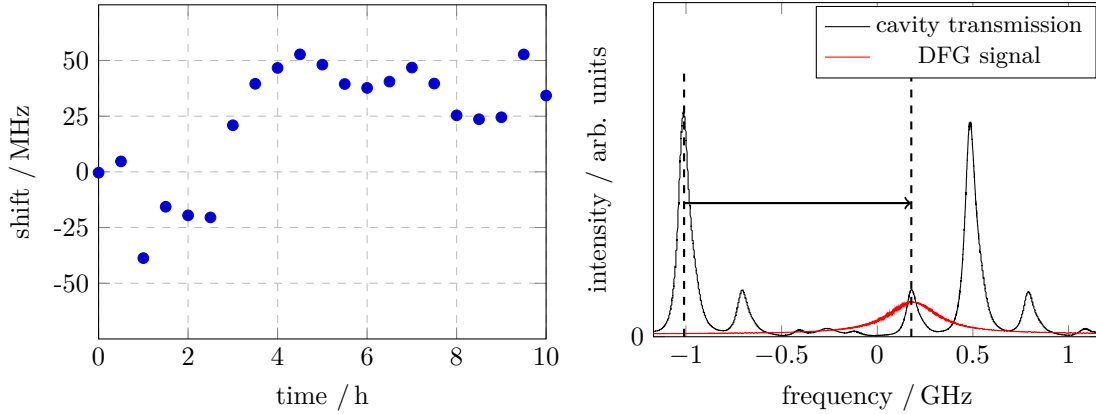


Figure 16: Frequency shifts of the reference cavity obtained by measurements taken every half hour over the course of 10 hours (left). We settled for one of the cavity transmission peaks as a reference point for the shift. Subsequently we compared this peak to all other measurements in order to calculate the overall cavity shift. The exact procedure on how to compensate for nonlinearities of the pump laser scan is described in the text. The DFG signal overlaid with the reference cavity spectrum modulated with sidebands at $\Omega \approx 1.2$ GHz and modulation depth of $\beta \approx 20$ dB (right). We scanned the 404 nm pump laser over about 2 GHz around the target frequency to visualize how the modulated pump sidebands are overlapped with the DFG signal in order to provide a locking point for the PID controller of the laser.

2.5 Heralding Efficiency

By switching the operation of the setup from DFG to SPDC, we expect much lower photon pair rates due to its spontaneous nature. In fact, for a pump power of about 3 mW, we measured signal and idler rates of $n_s = 5.8(6) \times 10^5$ counts/s and $n_i = 5.0(5) \times 10^4$ counts/s. In addition, by performing a series of measurements with different pump powers we found a signal-idler pair rate at $r = 5.4(5) \times 10^3$ pairs/(s mW) (Figure 17). This helped us determining the idler and signal efficiencies at $\eta_i = r/n_s = 2.8(3)\%$ and at $\eta_s = r/n_i = 29.2(3)\%$ respectively. Latter gives the likelihood of a signal photon located in the optical fiber upon an idler detection event which is called the heralding efficiency. Corrected for the detector efficiency of our devices at $\eta_{\text{det}} = 60(6)\%$, we find

$$\eta_{\text{heralded}} = \frac{r}{\eta_{\text{det}} n_i}. \quad (2.5.1)$$

We measured a consistent value at 53(5)% and without fine-tuning at 50(5)%. The heralding efficiency is a crucial measure in order to pair the source with a quantum memory since it shows the probability of a single photon located in the memory when announced by the idler, or herald. Consequently the memory can initiate the storage and retrieval process which is used for on-demand single photon generation. However, to run a memory successfully, it requires a high heralding efficiency which ensures that the memory readout remains non-classical. In order to keep the heralding efficiency high, the filtration is only performed in the herald arm. This also explains the significant lower idler count rates n_i . By doing so, we preselect photons at the target frequency, so that photons from other emission clusters cannot mistakingly announce any signal photons away from the target frequency. Even though the filtration is only performed in the idler arm both storage and detection of signal photons are not compromised by uncorrelated noise. The former because the atoms are highly sensitive to large detuning. The latter can be avoided for the same reason by a series of etalons.

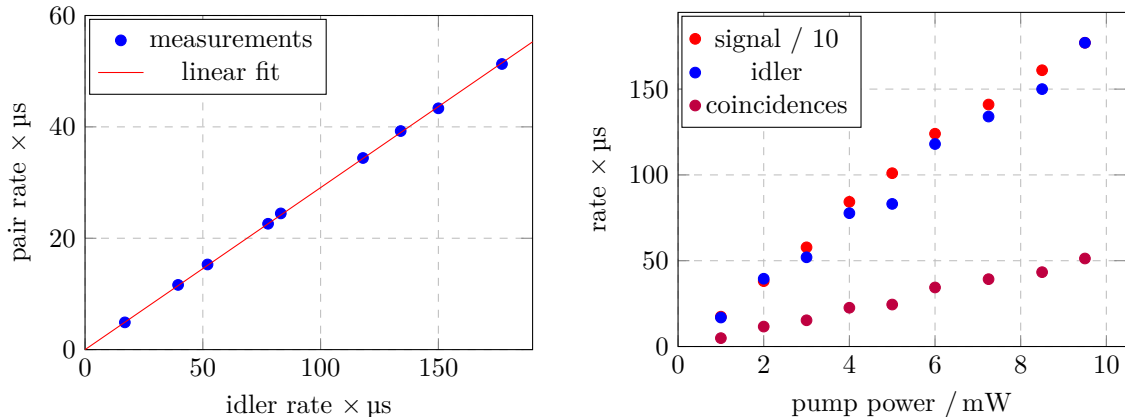


Figure 17: The signal-idler pair generation rate plotted against the idler rate for nine different power settings (left). The corresponding linear fit matches the measurements to an outstanding degree and we find the gradient to be the heralding efficiency at 29.2(3)% uncorrected for the detector efficiency. Different rates for signal, idler and coincidences are shown at different powers (right).

2.6 Second-Order Correlation Measurements

In order to quantify the single-photon character of the heralded single-photon source, we performed correlation measurements which show the photon statistics. For our experiments we use detectors exploiting the photo-electric effect referred to as single-photon avalanche detectors (SPAD, *Excelitas SPCM-AQRH-16*). We aligned them in an Hanbury Brown and Twiss (HBT) configuration containing detectors labeled S_1 and S_2 as well as the third detector situated in the other arm referred to as S_3 . Upon detection of a photon the detectors generate a short electrical pulse which feeds the time-tagger. The time-correlated single photon counting uses a single herald detection event and marks each subsequent signal detection event with a time stamp. This start-multistop counting procedure is needed to generate an histogram. Furthermore, the computer can add variable time delays among the channels in order to account for detection delays. It has been measured that our detectors in the HBT setup show a combined timing jitter of 1.72(4) ns [51]. However, since this characterization measurement we have been increasing degrees of freedom in order to improve the focus onto the detectors which should in return reduce the combined jitter. The time-tagger (*qtools quTau*) exhibit a minimum time resolution of $t_{\text{bin}} = 162\text{ps}$.

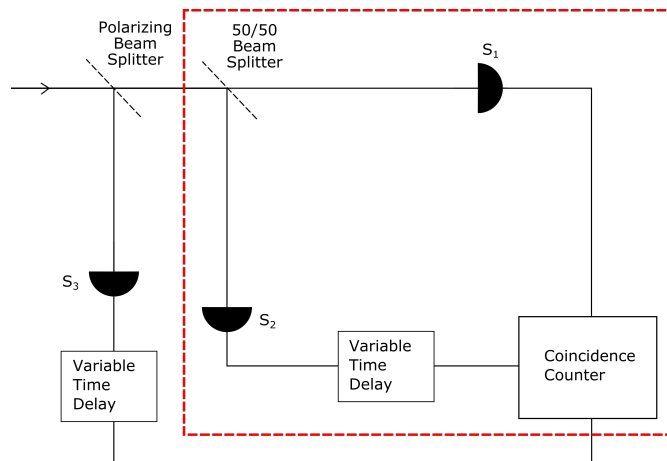


Figure 18: Experimental setup used to determine photon correlations of the SPDC heralded single-photon source. The red frame shows an HBT setup with two detectors (S_1 and S_2) connected to a coincidence counter. There is an additional time delay accounted for one of the arms in order to synchronize the correlation measurements. An additional detector (S_3) is needed to measure the crosscorrelation and the conditional autocorrelation.

The autocorrelation is a measure of the probability of photons to arrive bunched instead of independently. It can be accounted for by the second-order autocorrelation measure expressed in probabilities of coincidences P_{coin} and single-photon probabilities on either detector (P_{S_1}, P_{S_2}) and translate into measurable count rates on our detectors as:

$$g_{x,x}^{(2)} = \frac{P_{\text{coin}}}{P_{S_1} \cdot P_{S_2}} \approx \frac{n_{S_1, S_2} \cdot t_{\text{int}}}{n_{S_1} \cdot n_{S_2} \cdot t_{\text{bin}}} \quad (2.6.1)$$

where x stands for either signal or idler. The counts n_{S_1, S_2} and n_{S_1} (n_{S_2}) are the coincidence counts and total counts of the detectors S_1 (S_2), respectively, measured in a integration window of duration t_{int} . We expect both signal and idler arm to exhibit thermal statistics dictated by spontaneous parametric down-conversion [28]. This means the arms individually follow a Bose-Einstein distribution [54] and therefore show a feature which is often referred to as a bunching peak, so that $g_{x,x}^{(2)}(0) > 1$. In theory, this corresponds to Equation (1.6.3) for which we expect the autocorrelation for a single mode ($n=1$) to be 2. In order to generate the theory curve for the idler feature accounting for the setup components in Figure refAutoIdlerFigure (left), we convoluted the product of ideal idler lineshape of Equation (1.6.4) and the filter lineshapes with the IRF of the HBT setup. We used Lorentzians for idler (FWHM= 373 MHz) and etalon lineshapes (FWHM= 1.8 GHz) as well as a Gaussian IRF. In this process we found that the actual combined jitter of the HBT must be at 1.53 ns so that our measurements show a good agreement with the theory curve as depicted in Figure 19 (left). This indicates that the jitter could actually be reduced by improving the alignment. On the signal arm we find that the results are contaminated with other modes from the emission cluster (compare with Figure 14, right), washing out the thermal bunching feature. The idler photons, on the other hand, are not affected by contamination of other emission peaks but suffer from higher photon number events with increasing pump power. Higher number photon states also reduce the signal autocorrelation in Figure 19 (right) but the lack of filtration disguises its effect. Finally, comparing to what has been observed by Mottola et al. [51], we suspect to obtain better results due to the excellent pre-selection of the emission cluster.

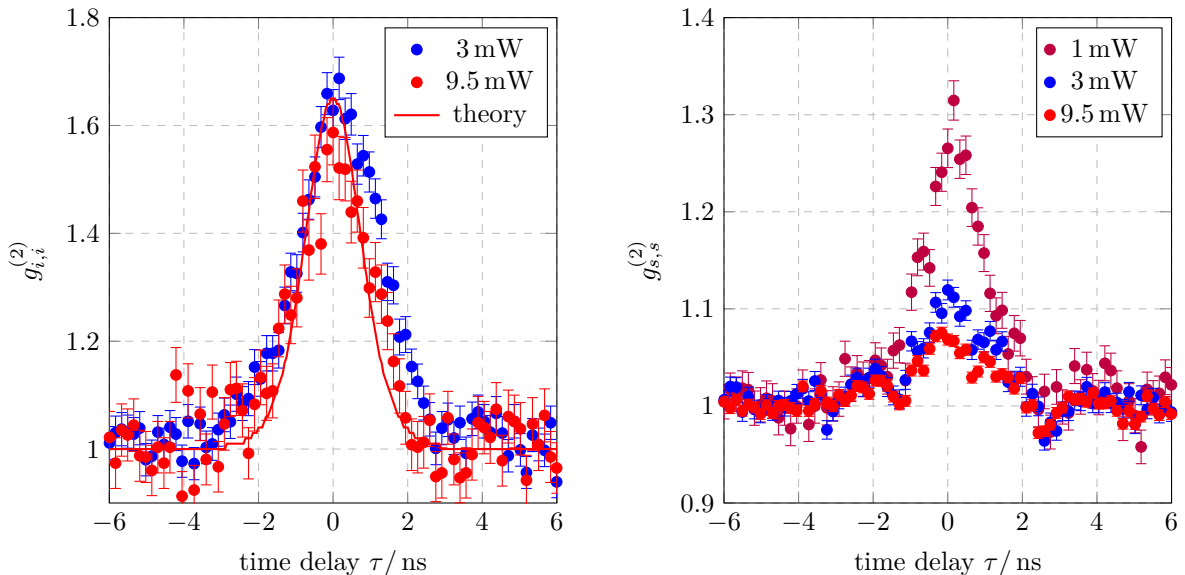


Figure 19: Second-order autocorrelation displayed for idler (left) and signal (right) photons. The idler photons show a very pronounced thermal bunching feature independently from its generation rate. On the other hand, the unfiltered signal photons show a diminishing thermal feature at higher pump powers due to the contamination of other modes. Since the ideal shape of the idler autocorrelation is given by Equation (1.6.4), the theory curve can be calculated as a product with the filter lineshape and convoluted with the IRF.

Conditioning the autocorrelation of signal photons on the detection of idler photons directly imposes the mode purity from the filtered idler photons onto the signal photons. Therefore, signal photons from other clusters are now only registered as uncorrelated noise. We gathered data for a series of different pump powers for which we each integrated over 80 bins to cover the whole thermal bunching feature in a coincidence window of $\Delta t = 6.48$ ns. In this time frame we measured the triple coincidence probability P_{triple} as well as the conditioned single photon detection probabilities on either of the HBT setup detectors ($P_{S_1,h}$, $P_{S_2,h}$). The conditional second-order autocorrelation can then be calculated theoretically with

$$g_c^{(2)} = \frac{P_{\text{triple}}}{P_{S_1,h} \cdot P_{S_2,h}} \approx \frac{(n_{S_1} + n_{S_2}) \cdot n_{S_1,S_2,h}}{n_{S_1,h} \cdot n_{S_2,h}}, \quad (2.6.2)$$

where $n_{S_1,S_2,h}$ and $n_{S_1,h}$ ($n_{S_2,h}$) are counts for triple coincidences and heralded events for SPAD S_1 (S_2) respectively. Its results are plotted against the pump power normalized generated pair rate $R = r/(P_{\text{pump}}\eta_s\eta_i) = n_i n_s / (r P_{\text{pump}}) = 6.5(7) \times 10^5$ pairs/(s mW) in Figure 20. We use the theory model proposed in Equation 24 of Sekatski et al. [74] while accounting for CW pumping in a regime far below threshold so that the photon generation can be estimated as $p \approx R P_{\text{pump}}$. Assuming no dark counts, which is a valid assumption considering that the dark counts are three orders of magnitude lower than generation rates, and corrected for the detector efficiency, the expression reads

$$g_c^{(2)} = 2RP_{\text{pump}}\Delta t - (RP_{\text{pump}}\Delta t)^2. \quad (2.6.3)$$

From Figure 20 we can estimate that the strong single-photon character $g_c^{(2)} < 0.01$ of the source remains for generation rates up to $7.5(8) \times 10^5$ pairs/s which corresponds to around 1 mW of pump power. The theory curve without any free parameters fits the measurements well.

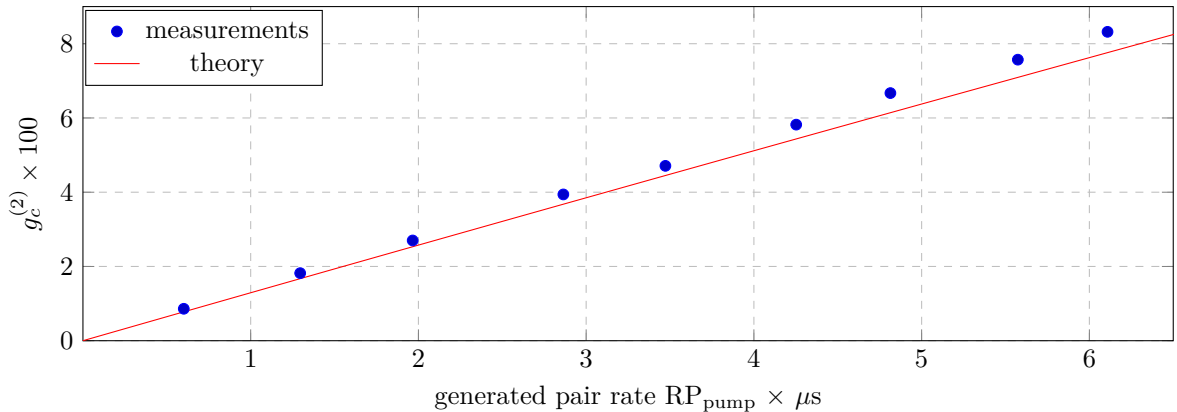


Figure 20: The second-order autocorrelation conditioned on an idler detection event integrated over 80 bins, that is a coincidence window of $t_{\text{bin}} = 6.48$ ns. It is visible that for higher pair rates the conditional autocorrelation increases linearly according to Equation (2.6.2) in the regime far below threshold. In other words, the source loses its single-photon character for higher pair generation rate. This particular source shows a $g_c^{(2)} < 0.01$ below generation rates of $7.5(8) \times 10^5$ pairs/s. The theory curve follows a model with no free parameters as presented in Equation (2.6.3). The error bars are smaller than the symbol size.

Another measure to test the heralded single photon source is the signal-idler-crosscorrelation. In simple terms, it shows the probability of a coincidence of signal and idler detection and can be written in terms of probabilities as

$$g_{s,i}^{(2)} = \frac{P_{\text{double}}}{(P_{S_1} + P_{S_2}) \cdot P_h} \approx \frac{n_{S_1,S_2} \cdot t_{\text{int}}}{(n_{S_1} + n_{S_2}) \cdot n_i \cdot t_{\text{bin}}}, \quad (2.6.4)$$

where P_{double} is the probability of a double coincidence between S_3 and either of S_1 or S_2 . The probability P_h is the probability to have a idler count on detector S_3 . From the crosscorrelation we expect the inverse behavior of the autocorrelation. At low pump power the detection of the generated pairs is not compromised. However, with increasing pump power the pair production rises and therefore the crosscorrelation faces increasing probability of contamination by other pairs and therefore decreases rapidly. This is also what we experimentally measured (see Figure 21) and which also matches well with the theory curve determined with the help of the Bayes's theorem giving a relation between the conditional autocorrelation and crosscorrelation:

$$g_c^{(2)} = \frac{g_{s,s}^{(2)} g_{i,i}^{(2)}}{g_{s,i}^{(2)}}, \quad (2.6.5)$$

where $g_c^{(2)}$ is governed by Equation (2.6.3). We hereby used that signal and idler autocorrelation behave equally and take into account that the idler autocorrelation over the coincidence window of 6.48 ns is $g_{i,i}^{(2)} = 1.28(5)$. This assumption is legitimate since we only take into account heralded signal photons which therefore inherited the idler photons' mode purity.

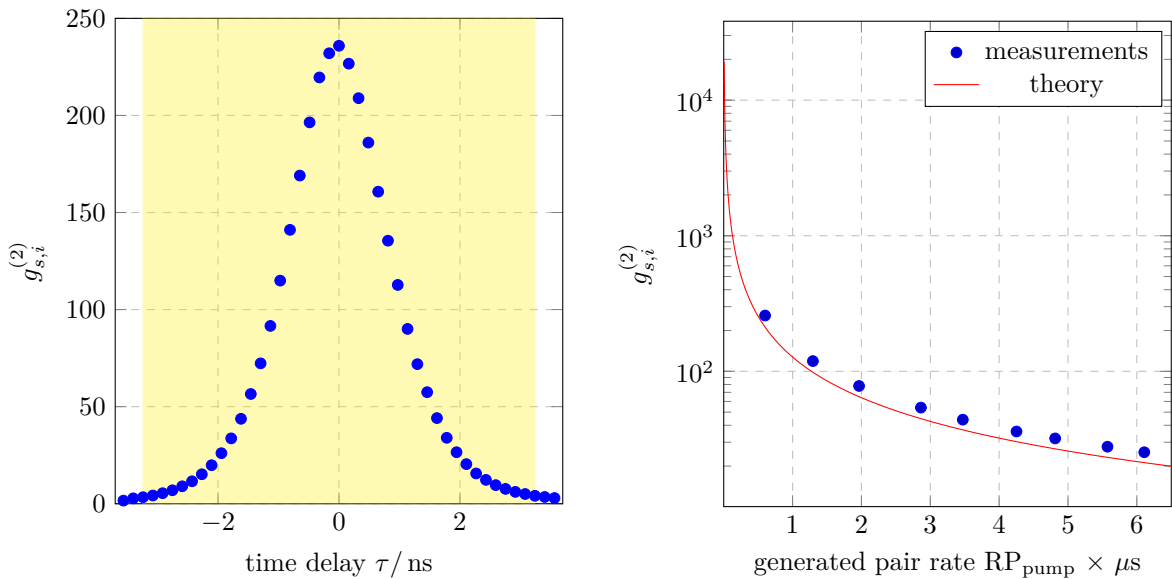


Figure 21: Measured second-order crosscorrelation at 3 mW for smallest bin size of $t_{\text{bin}} = 162$ ps dictated by the time-tagger (left). We observe pronounced bunching at $\tau = 0$ which implies that signal and idler are emitted in pairs. The fact that the peak is not infinitely small shows that both photons of a pair do not necessarily exit the crystal after the same number of round trips. Additionally, we find a slight asymmetry in the peak which originates in the dissimilar filtration of signal and idler photons. Especially the etalon in the idler arm spectrally narrows the idler photons which, in turn, are temporally widened. Its peak shape is determined by Equation 1.6.4. We would also expect a small effect induced by the wavelength and polarization dependent dielectric coatings of the crystal shaping the signal and idler photons differently (compare with Figure 2.28 in [75]). By evaluating the crosscorrelation over a coincidence window of $t_{\text{bin}} = 6.48$ ns (yellow shaded area of the figure on the left) we find a decreasing crosscorrelation for higher pair generation rates (right). The errorbars are smaller than the symbol size.

2.7 Backward Emitted Photons

Even though the emergence of photon pairs is strongly biased to one side, some still exit into the opposite direction and therefore negatively affect the photon statistics. By measuring the backwards emitted photons at a pump power of 7 mW we found $n_{s,\text{back}} = 1.5 \times 10^4$ signal photons/s while measuring 9.3×10^4 idler photons/s on the other side. Latter indicates that we would expect approximately 1.1×10^6 forwards emitted signal photons/s which results in 13% of all signal photons are being emitted backwards. We performed the measurement at the position for PD_1 in Figure 10 for which we could exclude any

losses since we used widely the same optics as in the signal arm. The only optics different from the signal arm, the shortpass filter, has been measured to exhibit negligible losses. Furthermore, according to the crosscorrelation measurement, depicted in Figure 22, the backward emitted photons are highly correlated to the idler photons emitted on the other side. In other words, these photons actually were generated in pairs but emerged the crystal in opposite directions. The ratio of backward emitted photons is far away from the targeted theoretical value for doubly resonant SPDC heralded single-photon sources with a lossless cavity [41]:

$$\eta(\omega) = \frac{1 - R_{s,i}^c}{1 - R_{s,i}^c R_{s,i}^p} = 1.2\%. \quad (2.7.1)$$

The variables $R_{s,i}^c$ and $R_{s,i}^p$ are the mirror reflectivities of the high reflective facet and the outcoupling facet respectively.

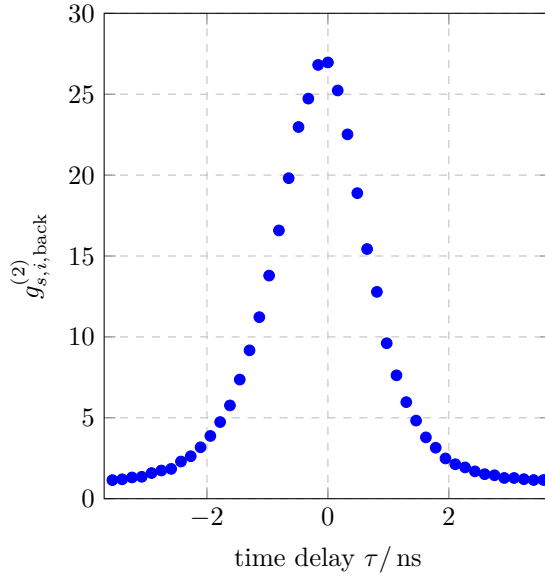


Figure 22: Signal-idler crosscorrelation measured for backward emitted signal photons. By correlating backward emitted photons with idler photons emitted on the opposite site, we find that they are highly correlated and therefore lose 13% of all signal photons through the other side of the crystal.

3 Discussion & Conclusion

In this thesis we presented a heralded single-photon source with significant improvements over the setup reported in Mottola et al. [51], which was designed to meet the requirements imposed by the quantum memory reported in Wolters et al. [48]. We adopted most parts of the design but omitted the reflective dielectric coating for the pump laser on the curved facet. By doing so, we abandoned the opportunity to lock the pump laser onto the crystal transmission modes. In exchange, we opted for a sideband offset lock on an external reference cavity. Losing the triple resonance condition makes strain tuning, which was an inconvenient degree of freedom due to its unidirectionality to begin with, superfluous. Similarly to temperature, strain caused, besides changes of the intra-crystal lattice, a variation of the dimensions of the crystal. As both temperature and strain acted on the cavity length, the phase-matching conditions could not be guaranteed. With the new design, which does not require mode matching for the pump beam within the crystal, we assume to have widely obviated gray-tracking of the crystal, which showed to be a central part of the crystal's deterioration [52]. This was a crucial part on improving the source's tuneability and robustness over the initial version.

The new source design outperforms the initial implementation in many aspects. One of the most prominent figures of merit for down-conversion sources, the heralding efficiency, could be increased by at least 8% to $\eta_{\text{heralded}} = 53(5)\%$. This can mostly be attributed to more careful pre-selection of the emission peaks of the cluster. However, this is still far away from the theoretical efficiency of 98.8% determined by Equation (2.7.1). We suspect multiple factors to account for this difference: First, even though the crystal is specified to be fully transparent at near infrared wavelengths [76], we cannot exclude absorption due to defects within the crystal lattice, causing signal photon losses. Additionally, highly reflective dielectric coatings are difficult to deposit on crystals and therefore may differ from their specified values [77]. Due to these inconsistent reflectivities the down-converted photons are increasingly likely to emerge from the curved side. This has been measured to account for 13% of all signal photons, leaving a maximum theoretical heralding efficiency of just 87% instead of 99%. By rearranging Equation (2.7.1) for the outcoupling facet's reflectivity, we find its dielectric coating to be short by only around 1% of the specified value. This difference also explains the discrepancies between theoretical and experimental values for the bandwidth of the signal photons. Finally, the two remaining arguments for low heralding efficiencies are losses in the fiber and its coupling. Prior has been specified with losses at 4 dB/km and the coupling exceeds an efficiency of 90%. Therefore they can be excluded to account for the remaining losses in the signal arm. Showing a detection efficiency of $\eta_{\text{det}} = 60(6)\%$, the single-photon detectors do not affect the heralding efficiency directly, but their error margins impose a relatively high uncertainty onto the results.

We also report improvements in the photon statistics of the source over the previous version. Specifically, we found good agreement for the idler second-order autocorrelation with the theory. Furthermore, we obtained satisfactory results for the signal autocorrelation which suggest that other peaks from the emission cluster do not contribute intensively to the overall cluster emission. Due to a lack of filtration, latter shows a strong power dependency on the bunching feature (compare with Figure 19) which is unsurprising given that other modes contribute progressively. Conditioning the signal autocorrelation upon an idler detection shows that the excellent single-photon character ($g_c^{(2)} < 0.01$) of the source is preserved up to a pair generation rate of 7.5×10^5 pairs/s. This is about 19% higher than what was measured for the first version of the source. Similarly, we observe a close to theory behavior of the crosscorrelation $g_{s,i}^{(2)}$ which naturally decays at higher pump powers. Additionally, we easily managed to achieve more efficient pumping of the crystal, as the initial version suffered from strong gray-tracking and therefore had to be operated off-resonantly.

We found the pump laser lock's performance not to be satisfying. As we opted for an external reference cavity we hoped to generate stable transmission modes to lock onto. Hemispherical cavity designs are proven to be robust against mirror misalignments and therefore served as an easy to implement option [73]. However, we found its finesse $\mathcal{F} = 8.6$ to be relatively low compared to its theoretical value of 40.3. We consulted the cavity stability condition

$$0 \leq \left(1 - \frac{L}{R_1}\right) \times \left(1 - \frac{L}{R_2}\right) \leq 1, \quad (3.0.1)$$

where R_1 and R_2 are the radii of curvature of mirror 1 and 2, respectively, and L is the cavity length, to find that the cavity stability is highly sensitive to the ratio of length over the radius of the curved mirror. For hemispherical cavities this ratio is unity by definition and thus marks the edge of the stability regime. If it increases above unity, the design falls out of the stability regime and becomes very fragile to operate in practice. We conclude that the cavity performance suffered from a slight mismatch of the length or discrepancies of mirror radii specifications. Yet we found that the Zerodur spacer provides stability over a 10 h time window with maximal drifts of 10 MHz/h.

Finally, we hope to benefit from better electronics in future versions. One of the critical points is the time-tagger's minimum time bin size. Even though it is specified to be as low as 81 ps, the effective minimum bin size is 162 ps due to an asymmetry of adjacent bin sizes. Lower bin sizes would allow for better resolution of the correlation measurements and hence better understanding of the photon statistics. Furthermore, it would grant better time alignment with the control pulse, when combined with the memory. Additionally, we note that the combined jitter of the HBT setup is greatly improved over the measurements in [51] but still requires some fine-tuning to achieve its theoretical minimum value of 0.55 ns.

In conclusion, we managed to narrow down the clusters most suitable for SPDC determined by the phase-matching conditions and cavity resonance. We started by operating the crystal at working parameters we designed the crystal for. Subsequently, by performing spectrometer measurements of the unseeded crystal paired with DFG fine-tuning, we could pinpoint the optimal cluster for which we could gather the optimal parameters for the crystal temperature at 29.3 °C and the pump laser wavelength at 404.218 nm. For a pump power of 3 mW we found signal and idler rates at $n_s = 5.8 \times 10^5$ counts/s and $n_i = 5.2 \times 10^4$ counts/s, respectively. The signal rate is much higher due to stringent filtration to a single emission line in the idler arm. Integrating over the time encompassing the entire thermal bunching feature, we found a signal-idler pair rate at $r = 15.3 \times 10^3$ counts/s, or 5.1×10^3 counts/(s mW) when normalized to the pump power. Consequently, we found a pair generation rate normalized to pump powers of $R = 6.5 \times 10^5$ pairs/(s mW), which is a 19% improvement over the initial version. Finally, we found that the emerging single photons show a bandwidth of 373(1) MHz, which is perfectly compatible with the acceptance bandwidth of the memory.

Outlook

Even though we are satisfied with the performance of the second iteration of the heralded single-photon source, there is still room for improvement. In the near future we plan to replace the flawed reference cavity. We decided to reuse the Zerodur cylinder since it showed promising long term stability. However, we will opt for mirrors with lower radii of curvature to ensure stability condition of Equation (3.0.1). With this we will significantly improve mode-matching in the cavity. This will allow us to implement a Pound-Drever-Hall lock for the pump laser. Specifically, we will operate it with sidebands of sidebands since the cavity is inherently not temperature-tuneable. Another change we intend to implement is an external mirror for the pump laser enabling a multipass pumping scheme. This should help to significantly increase generation rates at lower pump power. However, this new setup demands a more rigorous mode-matching alignment. While irradiating the same area of the crystal constantly, we hope to manage to preserve the crystal's improved lifespan.

In a series of experiments we could ensure the compatibility of source and quantum memory with respect to bandwidth, $g^{(2)}$, extraction efficiency, target frequency, and generation rate requirements. Therefore we are planning to implement the combined memory and source experiment in the near future. If we try to store a photon from this source with the quantum memory from Wolters et al. [48] we would expect to measure the weighted statistical mean

$$g_{\text{readout}}^{(2)} = \frac{g_{\text{noise}}^{(2)} + g_{\text{photon}}^{(2)} \cdot \text{SNR}}{\text{SNR} + 1} < 0.5, \quad (3.0.2)$$

for the readout photons with thermal noise and a SNR= 3.7(6). Yielding a sub-unity $g_{\text{readout}}^{(2)}$ shows that the retrieved photons remain non-classical which in turn suffices for a proof of principle experiment for the quantum memory.

Acknowledgments

First and foremost, I want to thank everyone who directly contributed to my master project. This includes on one hand Roberto Mottola and Gianni Buser who both provided me with valuable scientific practices and knowledge as well as interesting and funny non-science related facts. With an incredible time investment, they greatly contributed to the final thesis for which I will always be grateful for. Moreover, with their positive mood they created an enjoyable work atmosphere and I am glad that I can continue my work with them.

On the other hand, I owe a debt of gratitude to Prof. Dr. Philipp Treutlein, head of the quantum optics lab in Basel, who supported my project not only financially but also with his excellent mentorship. He was able to boost my motivation, gave me a great deal of freedom on the project and showed deep trust by discussing future working opportunities with me.

Furthermore, I want to thank the whole research group in Basel, which I am very happy to have had the opportunity to work with all of them. Despite Covid-19 measures the whole team held the spirit high and never missed the chance for a short chat in the hallway. I cherished the highly inspiring coffee breaks and Frisbee sessions in the park.

Of course, my gratefulness does not exclude Prof. Dr. Christophe Galland, Professor of the laboratory of quantum and nano optics at EPFL. His fantastic research group warmly welcomed me as an inexperienced master student and invested a lot of resources to teach me valuable lab practices. Moreover, I really appreciated the extraordinary team spirit and the fruitful discussions during coffee breaks. I want to thank Christophe Galland for these excellent opportunities on participating in all these semester projects under his supervision and for his great mentorship. During these three semesters, I acquired many new skills which I will cherish on my future career path.

Last but definitely not least I want to thank Josh Zuber from the research group of Prof. Dr. Maletinsky. He supported me during a critical stage of the experiment by helping me operate the spectrometer and generating spectra of Figures 14 and 13. He went above and beyond to help me, especially considering he too was at a very critical point of his PhD project. This is another great demonstration of how high teamwork is valued at the University of Basel.

4 References

- [1] T. H. Maiman, *Stimulated optical radiation in ruby*, Nature **187**, 493 (1960).
- [2] R. Horodecki, P. Horodecki, M. Horodecki, and K. Horodecki, *Quantum entanglement*, Reviews of Modern Physics **81**, 865 (2009).
- [3] J. P. Dowling and G. J. Milburn, *Quantum technology: the second quantum revolution*, Philosophical Transactions of the Royal Society of London. Series A: Mathematical, Physical and Engineering Sciences **361**, 1655 (2003).
- [4] T. D. Ladd, F. Jelezko, R. Laflamme, Y. Nakamura, C. Monroe, and J. L. O'Brien, *Quantum computers*, Nature **464**, 45 (2010).
- [5] V. Giovannetti, S. Lloyd, and L. Maccone, *Advances in quantum metrology*, Nature Photonics **5**, 222 (2011).
- [6] V. Scarani, H. Bechmann-Pasquinucci, N. J. Cerf, M. Dušek, N. Lütkenhaus, and M. Peev, *The security of practical quantum key distribution*, Reviews of Modern Physics **81**, 1301 (2009).
- [7] *Id Quantique*, www.idquantique.com.
- [8] *MagiQ Technologies*, www.magiqtech.com.
- [9] *Qnami*, www.qnami.ch.
- [10] D. P. Divincenzo, *The physical implementation of quantum computation*, Fortschritte der Physik **48**, 771 (2000).
- [11] N. Sangouard, C. Simon, H. de Riedmatten, and N. Gisin, *Quantum repeaters based on atomic ensembles and linear optics*, Reviews of Modern Physics **83**, 33 (2011).
- [12] F. Bussi eres, N. Sangouard, M. Afzelius, H. de Riedmatten, C. Simon, and W. Tittel, *Prospective applications of optical quantum memories*, Journal of Modern Optics **60**, 1519 (2013).
- [13] N. Gisin, G. Ribordy, W. Tittel, and H. Zbinden, *Quantum cryptography*, Review of Modern Physics **74**, 145 (2002).
- [14] A. Aspuru-Guzik and P. Walther, *Photonic quantum simulators*, Nature Physics **8**, 285 (2012).
- [15] P. Kok, W. J. Munro, K. Nemoto, T. C. Ralph, J. P. Dowling, and G. J. Milburn, *Linear optical quantum computing with photonic qubits*, Reviews of Modern Physics **79**, 135 (2007).
- [16] A. I. Lvovsky, B. C. Sanders, and W. Tittel, *Optical quantum memory*, Nature photonics **3**, 706 (2009).
- [17] C. Simon, M. Afzelius, J. Appel, A. B. de la Giroday, S. J. Dewhurst, N. Gisin, C. Y. Hu, F. Jelezko, S. Kroll, J. H. Muller, J. Nunn, E. Polzik, J. Rarity, H. de Riedmatten, W. Rosenfeld, A. J. Shields, N. Skold, R. M. Stevenson, R. Thew, I. Walmsley, M. Weber, H. Weinfurter, J. Wrachtrup, and R. J. Young, *Quantum memories. A review based on the european integrated project "qubit applications (qap)"*, The European Physical Journal D **58**, 1 (2010).
- [18] G. D. Fuchs, G. Burkard, P. V. Klimov, and D. D. Awschalom, *A quantum memory intrinsic to single nitrogen-vacancy centres in diamond*, Nature Physics **7**, 789 (2011).
- [19] P. C. Maurer, G. Kucsko, C. Latta, L. Jiang, N. Y. Yao, S. D. Bennett, F. Pastawski, D. Hunger, N. Chisholm, M. Markham, D. J. Twitchen, J. I. Cirac, and M. D. Lukin, *Room-temperature quantum bit memory exceeding one second*, Science **336**, 1283 (2012).
- [20] G. H etet, J. J. Longdell, A. L. Alexander, P. K. Lam, and M. J. Sellars, *Electro-optic quantum memory for light using two-level atoms*, Physical Review Letters **100**, 023601 (2008).
- [21] M. U. Staudt, S. R. Hastings-Simon, M. Nilsson, M. Afzelius, V. Scarani, R. Ricken, H. Suche, W. Sohler, W. Tittel, and N. Gisin, *Fidelity of an optical memory based on stimulated photon echoes*, Physical Review Letters **98**, 113601 (2007).

- [22] D. L. Moehring, P. Maunz, S. Olmschenk, K. C. Younge, D. N. Matsukevich, L.-M. Duan, and C. Monroe, *Entanglement of single-atom quantum bits at a distance*, Nature **449**, 68 (2007).
- [23] T. Wilk, S. C. Webster, A. Kuhn, and G. Rempe, *Single-atom single-photon quantum interface*, Science **317**, 488 (2007).
- [24] B. Zhao, Y.-A. Chen, X.-H. Bao, T. Strassel, C.-S. Chuu, X.-M. Jin, J. Schmiedmayer, Z.-S. Yuan, S. Chen, and J.-W. Pan, *A millisecond quantum memory for scalable quantum networks*, Nature Physics **5**, 95 (2009).
- [25] T. Chaneliere, D. N. Matsukevich, S. D. Jenkins, S. Y. Lan, T. A. B. Kennedy, and A. Kuzmich, *Storage and retrieval of single photons transmitted between remote quantum memories*, Nature **438**, 833836 (2005).
- [26] K. F. Reim, J. Nunn, V. O. Lorenz, B. J. Sussman, K. C. Lee, N. K. Langford, D. Jaksch, and I. A. Walmsley, *Towards high-speed optical quantum memories*, Nature Photonics **4**, 218 (2010).
- [27] D. J. Saunders, J. H. D. Munns, T. F. M. Champion, C. Qiu, K. T. Kaczmarek, E. Poem, P. M. Ledingham, I. A. Walmsley, and J. Nunn, *Cavity-enhanced room-temperature broadband Raman memory*, Physical Review Letters **116**, 090501 (2016).
- [28] N. Somaschi, V. Giesz, L. De Santis, J. C. Loredo, M. P. Almeida, G. Hornecker, S. L. Portalupi, T. Grange, C. Antón, J. Demory, C. Gómez, I. Sagnes, N. D. Lanzillotti-Kimura, A. Lemaitre, A. Auffeves, A. G. White, L. Lanco, and P. Senellart, *Near-optimal single-photon sources in the solid state*, Nature Photonics **10**, 340 (2016).
- [29] C. Santori, D. Fattal, J. Vukovi, G. S. Solomon, and Y. Yamamoto, *Indistinguishable photons from a single-photon device*, Nature **419**, 594 (2002).
- [30] S. Ates, S. M. Ulrich, A. Ulhaq, S. Reitzenstein, A. Löffler, S. Höfling, A. Forchel, and P. Michler, *Non-resonant dotcavity coupling and its potential for resonant single-quantum-dot spectroscopy*, Nature Photonics **3**, 724 (2009).
- [31] R. M. Stevenson, R. J. Young, P. Atkinson, K. Cooper, D. A. Ritchie, and A. J. Shields, *A semiconductor source of triggered entangled photon pairs*, Nature **439**, 179 (2006).
- [32] Y. Chen, J. Zhang, M. Zopf, K. Jung, Y. Zhang, R. Keil, F. Ding, and O. G. Schmidt, *Wavelength-tunable entangled photons from silicon-integrated III-V quantum dots*, Nature Communications **7**, 10387 (2016).
- [33] P. Senellart, G. Solomon, and A. White, *High-performance semiconductor quantum-dot single-photon sources*, Nature Nanotechnology **12**, 1026 (2017).
- [34] A. Reigue, J. Iles-Smith, F. Lux, L. Monniello, M. Bernard, F. Margaiilan, A. Lemaitre, A. Martinez, D. P. S. McCutcheon, J. Mørk, R. Hostein, and V. Voliotis, *Probing electron-phonon interaction through two-photon interference in resonantly driven semiconductor quantum dots*, Physical Review Letters **118**, 233602 (2017).
- [35] A. Thoma, P. Schnauber, M. Gschrey, M. Seifried, J. Wolters, J.-H. Schulze, A. Strittmatter, S. Rodt, A. Carmele, A. Knorr, T. Heindel, and S. Reitzenstein, *Exploring dephasing of a solid-state quantum emitter via time- and temperature-dependent Hong-Ou-Mandel experiments*, Physical Review Letters **116**, 033601 (2016).
- [36] L. Béguin, J.-P. Jahn, J. Wolters, M. Reindl, Y. Huo, R. Trotta, A. Rastelli, F. Ding, O. G. Schmidt, P. Treutlein, and R. J. Warburton, *On-demand semiconductor source of 780-nm single photons with controlled temporal wave packets*, Physical Review B **97**, 205304 (2018).
- [37] P. Lodahl, *Quantum-dot based photonic quantum networks*, Quantum Science and Technology **3**, 013001 (2017).
- [38] M. Scholz, L. Koch, and O. Benson, *Statistics of narrow-band single photons for quantum memories generated by ultrabright cavity-enhanced parametric down-conversion*, Physical Review Letters **102**, 063603 (2009).

- [39] A. Ahlrichs and O. Benson, *Bright source of indistinguishable photons based on cavity-enhanced parametric down-conversion utilizing the cluster effect*, Applied Physics Letters **108**, 021111 (2016).
- [40] J. Fekete, D. Rieländer, M. Cristiani, and H. de Riedmatten, *Ultrannarrow-band photon-pair source compatible with solid state quantum memories and telecommunication networks*, Physical Review Letters **110**, 220502 (2013).
- [41] K.-H. Luo, H. Herrmann, S. Krapick, B. Brecht, R. Ricken, V. Quiring, H. Suche, W. Sohler, and C. Silberhorn, *Direct generation of genuine single-longitudinal-mode narrowband photon pairs*, New Journal of Physics **17**, 073039 (2015).
- [42] C.-S. Chuu, G. Y. Yin, and S. E. Harris, *A miniature ultrabright source of temporally long, narrow-band biphotons*, Applied Physics Letters **101**, 051108 (2012).
- [43] A. L. Migdall, D. Branning, and S. Castelletto, *Tailoring single-photon and multiphoton probabilities of a single-photon on-demand source*, Physical Review A **66**, 053805 (2002).
- [44] L.-K. Chen, Z.-D. Li, X.-C. Yao, M. Huang, W. Li, H. Lu, X. Yuan, Y.-B. Zhang, X. Jiang, C.-Z. Peng, L. Li, N.-L. Liu, X. Ma, C.-Y. Lu, Y.-A. Chen, and J.-W. Pan, *Observation of ten-photon entanglement using thin BiB₃O₆ crystals*, Optica **4**, 77 (2017).
- [45] M. Tillmann, B. Dakić, R. Heilmann, S. Nolte, A. Szameit, and P. Walther, *Experimental boson sampling*, Nature photonics **7**, 540 (2013).
- [46] J. B. Spring, B. J. Metcalf, P. C. Humphreys, W. S. Kolthammer, X.-M. Jin, M. Barbieri, A. Datta, N. Thomas-Peter, N. K. Langford, D. Kundys, J. C. Gates, B. J. Smith, P. G. R. Smith, and I. A. Walmsley, *Boson sampling on a photonic chip*, Science **339**, 798 (2013).
- [47] D. E. Browne and T. Rudolph, *Resource-efficient linear optical quantum computation*, Physical Review Letters **95**, 010501 (2005).
- [48] J. Wolters, G. Buser, A. Horsley, L. Béguin, A. Jöckel, J.-P. Jahn, R. J. Warburton, and P. Treutlein, *Simple atomic quantum memory suitable for semiconductor quantum dot single photons*, Physical Review Letters **119**, 060502 (2017).
- [49] J.-P. Jahn, M. Munsch, L. Béguin, A. V. Kuhlmann, M. Renggli, Y. Huo, F. Ding, R. Trotta, M. Reindl, O. G. Schmidt, A. Rastelli, P. Treutlein, and R. J. Warburton, *An artificial Rb atom in a semiconductor with lifetime-limited linewidth*, Physical Review B **92**, 245439 (2015).
- [50] G. Buser, *Atomic quantum memory for broadband single photons*, Ph.D. thesis, Universität Basel, to be published.
- [51] R. Mottola, G. Buser, C. Müller, T. Kroh, A. Ahlrichs, S. Ramelow, O. Benson, P. Treutlein, and J. Wolters, *An efficient, tunable, and robust source of narrow-band photon pairs at the ⁸⁷Rb D₁ line*, Optics Express **28**, 3159 (2020).
- [52] B. Boulanger, I. Rousseau, J.-p. Feve, M. Maglione, B. Ménaert, and G. Marnier, *Optical studies of laser-induced gray-tracking in KTP*, Quantum Electronics, IEEE Journal of **35**, 281 (1999).
- [53] R. Loudon, *The quantum theory of light*, , Oxford science publications (Oxford University Press), 3rd edition edition (2000).
- [54] P. W. Milonni and J. H. Eberly, *Laser physics*, (Wiley-Blackwell, Oxford) (2010).
- [55] R. Boyd and B. Masters, *Nonlinear optics*, volume 14 (Academic Press), 3rd edition edition (2009).
- [56] P. E. Powers and J. W. Haus, *Fundamentals of nonlinear optics*, (CRC Press) (2017).
- [57] F. A. Laudembach, *Engineering spectrally pure quantum states with SPDC using periodically poled crystals and pulsed laser sources*, Master's thesis, Universität Wien (2015).
- [58] K. Fradkin, A. Arie, A. Skliar, and G. Rosenman, *Tunable midinfrared source by difference frequency generation in bulk periodically poled KTiOPO₄*, Applied Physics Letters **74**, 914 (1999).

- [59] D. A. Kleinman, *Nonlinear dielectric polarization in optical media*, Physical Review **126**, 1977 (1962).
- [60] S. Reynaud, A. Lambrecht, C. Genet, and M.-T. Jaekel, *Quantum vacuum fluctuations*, Comptes Rendus de l'Académie des Sciences-Series IV-Physics **2**, 1287 (2001).
- [61] S. Reynaud and A. Heidmann, *A semiclassical linear input output transformation for quantum fluctuations*, Optics Communications **71**, 209 (1989).
- [62] O. Roslyak and S. Mukamel, *A unified description of sum frequency generation, parametric down conversion and two-photon fluorescence*, Molecular physics **107**, 265 (2009).
- [63] J. A. Armstrong, N. Bloembergen, J. Ducuing, and P. S. Pershan, *Interactions between light waves in a nonlinear dielectric*, Physical Review **127**, 1918 (1962).
- [64] A. Vanselow, P. Kaufmann, H. Chrzanowski, and S. Ramelow, *Ultra-broadband SPDC for spectrally far separated photon pairs*, Optics Letters **44**, 4638 (2019).
- [65] R. J. Glauber, *The quantum theory of optical coherence*, Physical Review **130**, 2529 (1963).
- [66] A. Christ, K. Laiho, A. Eckstein, K. N. Cassemiro, and C. Silberhorn, *Probing multimode squeezing with correlation functions*, New Journal of Physics **13**, 033027 (2011).
- [67] K. J. McNeil and C. W. Gardiner, *Quantum statistics of parametric oscillation*, Physal Review A **28**, 1560 (1983).
- [68] T. Lettau, H. Leymann, B. Melcher, and J. Wiersig, *Superthermal photon bunching in terms of simple probability distributions*, Physical Review A **97** (2018).
- [69] C. Gerry and P. Knight, *Introductory quantum optics*, (Cambridge University Press) (2004).
- [70] D. Steck, *Rubidium 87 D line data* (2003).
- [71] F. Kaneda, K. Garay-Palmett, A. B. U'Ren, and P. G. Kwiat, *Heralded single-photon source utilizing highly nondegenerate, spectrally factorable spontaneous parametric downconversion*, Optics express **24**, 10733 (2016).
- [72] H. Zhang, X.-M. Jin, J. Yang, H.-N. Dai, S.-J. Yang, T.-M. Zhao, J. Rui, Y. He, X. Jiang, F. Yang *et al.*, *Preparation and storage of frequency-uncorrelated entangled photons from cavity-enhanced spontaneous parametric downconversion*, Nature Photonics **5**, 628 (2011).
- [73] W. Koechner, *Solid-state laser engineering*, (Springer) (2006).
- [74] P. Sekatski, N. Sangouard, F. Bussi eres, C. Clausen, N. Gisin, and H. Zbinden, *Detector imperfections in photon-pair source characterization*, Journal of Physics B: Atomic, Molecular and Optical Physics **45**, 124016 (2012).
- [75] A. Ahlrichs, *Triply-resonant cavity-enhanced spontaneous parametric down-conversion*, Ph.D. thesis, Humboldt-Universit at (2019).
- [76] J. D. Bierlein and H. Vanherzeele, *Potassium titanyl phosphate: properties and new applications*, Journal of the Optical Society of America B **6**, 622 (1989).
- [77] J. Borchers, *Managing director of Lens-Optics*, private communication (2018).
- [78] M. Scholz, *New light sources for quantum information processing*, Ph.D. thesis, Humboldt-Universit at (2009).
- [79] P. J. Mosley, *Generation of heralded single photons in pure quantum states*, Ph.D. thesis, University of Oxford (2007).
- [80] S. Emanuelli and A. Arie, *Temperature-dependent dispersion equations for KTiOPO₄ and KTiOAsO₄*, Applied Optics **42**, 6661 (2003).

- [81] T. Y. Fan, C. E. Huang, B. Q. Hu, R. C. Eckardt, Y. X. Fan, R. L. Byer, and R. S. Feigelson, *Second harmonic generation and accurate index of refraction measurements in flux-grown $KTiOPO_4$* , *Applied Optics* **26**, 2390 (1987).
- [82] D. L. Fenimore, K. L. Schepler, U. B. Ramabadran, and S. R. McPherson, *Infrared corrected Sellmeier coefficients for potassium titanyl arsenate*, *Journal of the Optical Society of America* **12**, 794 (1995).
- [83] Z. Zhong, P. Gallagher, D. Loiacono, and G. Loiacono, *The thermal expansion and stability of $KTiOAsO_4$ and related compounds*, *Thermochimica Acta* **234**, 255 (1994).
- [84] D. N. Nikogosyan, *Nonlinear optical crystals: a complete survey*, (Springer Science & Business Media) (2006).

Appendix A Ray Transfer Matrix Analysis for Cavity Mode-Matching

Every optical cavity supports spatial modes for which the wavefronts match the cavity geometry. In order to match these constraints the waves outside the cavity have to be changed accordingly. This can be done by taking optics such as mirrors or lenses. The ray transfer matrix analysis (RTMA) provides a viable mathematical tool accounting for Gaussian beam propagation and allowing to match the modes to the supported cavity modes. However, it is useful to first establish formulas for Gaussian optics [54]:

$$w(z) = w_0 \sqrt{1 + \left(\frac{z}{z_R}\right)^2}, \quad (\text{A.0.1})$$

for the beam $1/e$ radius at a distance z , with z_R as the Rayleigh length

$$z_R = \frac{\pi w_0^2 n}{\lambda}, \quad (\text{A.0.2})$$

the distance at which the beam size is $\sqrt{2}w_0$. The beam waist radius w_0 accounts for the minimal beam radius of the Gaussian beam as illustrated in Figure A.0.5. Furthermore, the radius of curvature of the wavefronts is given by

$$R(z) = z \left(1 + \frac{z_R}{z}\right). \quad (\text{A.0.3})$$

These expressions help to understand the formulas provided for RTMA. One formula of particular interest is the one for the complex beam parameter q :

$$\frac{1}{q} = \frac{1}{R} - i \frac{\lambda}{\pi n w^2}, \quad (\text{A.0.4})$$

which allows together with the $ABCD$ matrix [54] to calculate beam parameter at a transition interface:

$$\begin{pmatrix} q_2 \\ 1 \end{pmatrix} = k \begin{pmatrix} A & B \\ C & D \end{pmatrix} \begin{pmatrix} q_1 \\ 1 \end{pmatrix}. \quad (\text{A.0.5})$$

We labeled the complex beam parameters before and after the interface with q_1 and q_2 respectively. The coefficients A , B , C , and D are entries of the $ABCD$ matrix for Gaussian beam propagation. Its shape and its numerical values are determined by the kind of interface [54].

In this section of the appendix we discuss three cases for which we applied the RTMA method to find the optimal specifications for our optics. The first case describes the mode coupling of the 795 nm seed laser into the crystal impinging on the planar facet. The second case describes the mode coupling of the pump laser from the opposite site. This is arguably obsolete since the crystal does not form a resonator for the blue pump light. However, we can still use the results to install the optics accordingly to improve the pumping. Last, we introduce a case for our plans to implement a mirror for the pump light to finally form an optical resonator. Since we already have a curved mirror we perform these calculations with the radius of curvature as a constraint.

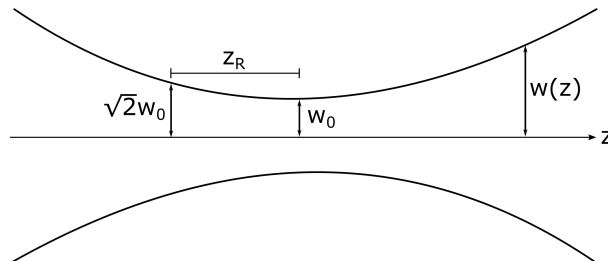


Figure 23: Visual representation of Gaussian beam propagation. The Rayleigh length z_R is defined as the distance between the beam origin ($z = 0$) and the distance at which beam spot is twice the spot size of the focal point spot size.

Case 1

In the first case we are using RTMA to determine the focal length f of a lens used to couple the seed laser ($\lambda_s = 795 \text{ nm}$) into the crystal on the planar facet which is needed to match the cavity mode. We start by determining the beam waist with the help of Equation (A.0.3) and the fact that the beam radius matches the radius of curvature of the curved facet:

$$w_0 = \sqrt{\frac{z\lambda_s}{n_{\text{cr}}\pi} \sqrt{\frac{R}{L} - 1}}. \quad (\text{A.0.6})$$

Inserting numerical values for the radius of curvature of the curved facet $R = 10 \text{ mm}$, the crystal length $L = 5 \text{ mm}$, and the crystal's refractive index $n_{\text{cr}} \approx 1.95$ yields

$$w_0 = 25.47 \mu\text{m}. \quad (\text{A.0.7})$$

By employing Equation (A.0.1) and the definition for the Rayleigh length (A.0.2) we find the focal length of the lens for a pump beam size of $w(z) = 1050 \mu\text{m}$

$$z = f = \sqrt{\left[\left(\frac{w(z)}{w_0}\right)^2 - 1\right] z_R} = 105.66 \text{ mm}. \quad (\text{A.0.8})$$

In other words we require a $f \approx 100 \text{ mm}$ lens to achieve mode-matching with our current pump beam profile.

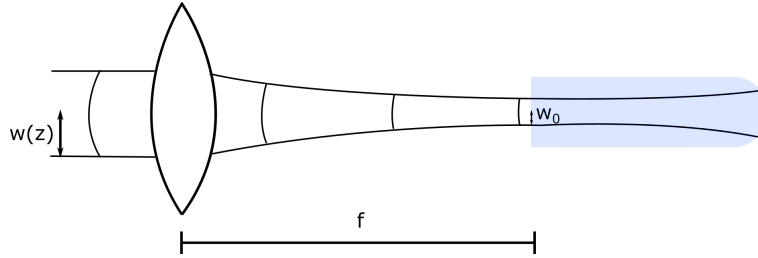


Figure 24: Schematics of the situation in case 1. With the help of a lens we can match the mode profile within the crystal. The calculation steps to determine the focal length f required to match the mode to the cavity mode are described in the text.

Case 2

This case describes the mode-matching process to couple the pump beam to the crystal through the curved facet. Similar to case 1, we determined the waist size for the beam which can be found for $\lambda_p = 405 \text{ nm}$ to be $w_0 = 18.18 \text{ }\mu\text{m}$. Together with the Rayleigh length of the beam which is determined with Equation (A.0.2) as 5 mm , we find the beam size at the curved facet to be $25.71 \text{ }\mu\text{m}$. These results allow us to employ calculations with the complex Gaussian beam parameter which are fundamental for the RTMA. The complex beam parameter of the beam at the curved facet within the crystal (see Figure 25) reads

$$q_2 = \frac{1}{\frac{1}{R} - i\frac{\lambda}{\pi n_{\text{cr}} w^2}}. \quad (\text{A.0.9})$$

The $ABCD$ matrix for the curved crystal-air interface is given by [54]

$$\begin{pmatrix} A & B \\ C & D \end{pmatrix} = \begin{pmatrix} 1 & 0 \\ \frac{n_{\text{air}} - n_{\text{cr}}}{R n_{\text{cr}}} & \frac{n_{\text{air}}}{n_{\text{cr}}} \end{pmatrix}, \quad (\text{A.0.10})$$

with the air's refractive index $n_{\text{air}} \approx 1$ and the beam's radius of curvature R negative by convention. Consequently, the complex beam parameter is calculated by solving Equation (A.0.5) with the entries for the $ABCD$ as

$$q_3 = \frac{q_2}{\frac{n_{\text{cr}} - n_{\text{air}}}{R n_{\text{air}}} + \frac{n_{\text{cr}}}{n_{\text{air}}}}. \quad (\text{A.0.11})$$

In order to now estimate the distance between the crystal-air interface and the lens (labeled as d_2 in Figure 25) we need to define the collimated beam size after the lens. For our case this coincides with the beam radius of the pump laser measured at $500 \text{ }\mu\text{m}$. Using the $ABCD$ matrix for free space propagation from [54]

$$\begin{pmatrix} A & B \\ C & D \end{pmatrix} = \begin{pmatrix} 1 & d_2 \\ 0 & 1 \end{pmatrix} \quad (\text{A.0.12})$$

yields a complex beam parameter

$$q_4 = q_3 + d_2. \quad (\text{A.0.13})$$

Comparing its imaginary part to the one obtained with Equation (A.0.4) we find distance d_2 as depicted in Figure 25 as

$$d_2 = 86.56 \text{ mm}. \quad (\text{A.0.14})$$

Note that the distance d_2 together with the crystal length do not sum up to the lens' focal length. In fact, the crystal shifts stretches the focal length with its refractive index higher than air further in the crystal to

$$f = \frac{L}{n_{\text{cr}}} + d_2. \quad (\text{A.0.15})$$

This situation is depicted in Figure 25 (right).

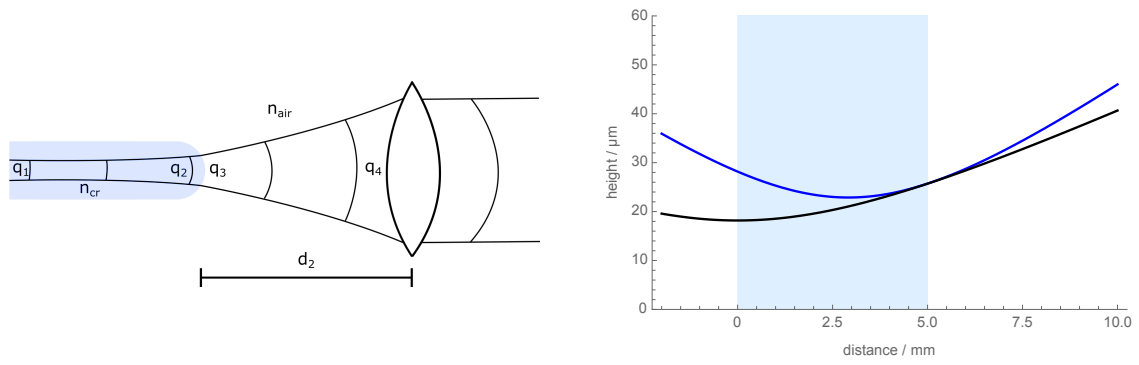


Figure 25: The situation schematics for case 2 for pump laser mode-matching depicted on the left. We perform a series of measurement in order to find the focal length for a lens suitable to match the pump mode to the cavity mode. In return we find the the distance labeled as d_2 which added with the crystal length corresponds approximately. However, the free space focal length (depicted in blue on the right) of the lens falls short by some millimeters in contrast to the combined crystal-air configuration (black).

Case 3

This case is used for a possible iteration of the source which uses an extra mirror to form a cavity for the pump beam too (illustrated in Figure 26, left). It is meant to recycle pump light which in return increases the pair generation rate. However, the Gaussian nature of the beam requires a careful RTMA for mirror positioning to enable mode-matching. This configuration poses two constraints for the mode-matching: The beam curvature must be identical to the facet curvature ($R=10$ mm) at the crystal-air interface so that the wavefront matches the crystals geometry in order to be supported by the cavity. When exited the cavity, the wavefront must additionally fit the mirror curvature ($R = 25$ mm) at a distance z away from the crystal. The curvature of the mirror has been chosen for convenience. Fortunately, case 2 already provides the complex beam parameter which is needed for this problem. Harnessing Equation (A.0.4) yields two solutions, both at opposite prefix. Considering only positive solutions yields

$$d_3 = 22.2 \text{ mm.} \quad (\text{A.0.16})$$

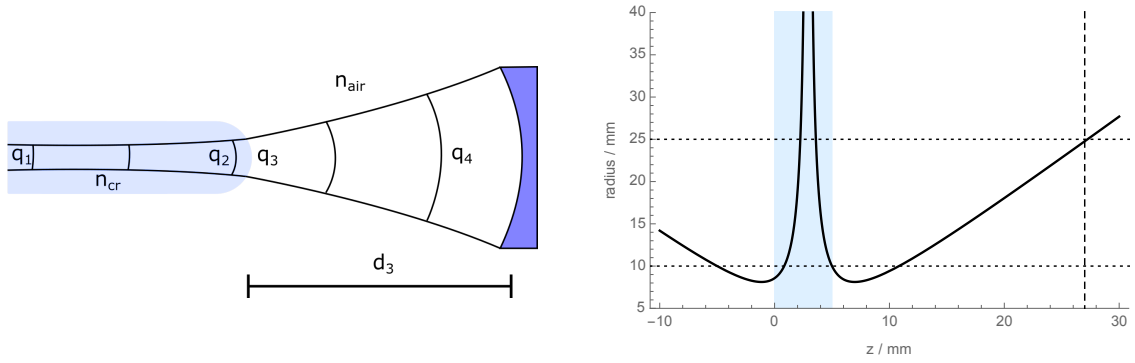


Figure 26: This schematic shows the situation of case 3 (left). By adding an external mirror with high reflective dielectric coatings for 404 nm we can form a resonator for the pump beam. The mode-matching, required for a satisfying mode profile, dictates the placement of a mirror with radius of curvature $R = 25$ mm (right) when only considering positive solutions. A negative solution would have suggested a mirror placement on the opposite site of the crystal.

Appendix B Refractive Indices of KTP

Potassium titanyl phosphate, or KTP, is a biaxial crystal which shows transparency in the window of 350 nm to 4.5 μm [76]. The general temperature-dependent shape of the refractive index has been found by [80] as

$$n(\lambda, T) = n(\lambda) + \Delta n(\lambda, T), \quad (\text{B.0.1})$$

where the first term corresponds to the refractive index at room temperature (25°C). It is determined by Equation 1.1.15 for the ordinary (z) axis with coefficients $A = 2.19229$, $B = 0.83547$, $C = 0.04970$, and $D = 2.25411$, and for the extraordinary (y) axis by the Sellmeier equation proposed by Fan et al. [81] as

$$n^2 = A + \frac{B}{1 - C/\lambda^2} - D\lambda^2, \quad (\text{B.0.2})$$

with coefficients $A = 2.19229$, $B = 0.83547$, $C = 0.04970$, and $D = 0.01621$. The second term of Equation B.0.1 yields a correction term for any temperatures different than 25°C given by Emanuelli et al. [80]

$$\Delta n(\lambda, T) = n_1(\lambda)(T - 25^\circ\text{C}) + n_2(\lambda)(T - 25^\circ\text{C})^2, \quad (\text{B.0.3})$$

with the parabolic coefficients n_1 and n_2 determined by a third-order polynomial of negative powers of the wavelength [82]:

$$n_{1,2}(\lambda) = \sum_{m=0}^3 \frac{a_m}{\lambda^m}. \quad (\text{B.0.4})$$

Its empirically determined coefficients a_m are listed in Table 1.

Furthermore, Zhong et al. [83] claimed a parabolic dependence on temperature for the thermal expansion of the crystal:

$$L = L_0(1 + \alpha(T - 25^\circ\text{C}) + \beta(T - 25^\circ\text{C})^2), \quad (\text{B.0.5})$$

with coefficients $\alpha = 7.7 \times 10^{-6} \text{ }^\circ\text{C}^{-1}$ and $\beta = 7.1 \times 10^{-9} \text{ }^\circ\text{C}^{-2}$.

	ordinary		extraordinary	
	n_1 [10^{-6}]	n_2 [10^{-8}]	n_1 [10^{-6}]	n_2 [10^{-8}]
a_0	9.9587	-1.1882	6.2897	-0.14445
a_1	9.9228	10.459	6.3061	2.2244
a_2	-8.9603	-9.8136	-6.0629	-3.5770
a_3	4.1010	3.1481	2.6486	1.3470

Table 1: These are the coefficients for the parabolic coefficients n_1 and n_2 which are used to determine the temperature depend refractive index proposed by Emanuelli et al. [80].

Appendix C Crystal Properties of KTP

Without loss of generality the second-order nonlinear polarization can be expressed as

$$\mathbf{P}_{\text{tot}}^{(2)} = \epsilon_0 d_{jk} \mathbf{E}_{\text{tot},j} \mathbf{E}_{\text{tot},k}, \quad (\text{C.0.1})$$

with

$$\mathbf{E}_{\text{tot}} = \mathbf{E}(\omega_p) + \mathbf{E}(\omega_s) + \mathbf{E}(\omega_i). \quad (\text{C.0.2})$$

By rewriting it in vector notation we obtain:

$$\begin{pmatrix} P_x \\ P_y \\ P_z \end{pmatrix} = 2\epsilon_0 \begin{pmatrix} d_{11} & d_{12} & d_{13} & d_{14} & d_{15} & d_{16} \\ d_{21} & d_{22} & d_{23} & d_{24} & d_{25} & d_{26} \\ d_{31} & d_{32} & d_{33} & d_{34} & d_{35} & d_{36} \end{pmatrix} \begin{pmatrix} E_x^2 \\ E_y^2 \\ E_z^2 \\ 2E_y E_z \\ 2E_z E_x \\ 2E_x E_y \end{pmatrix}. \quad (\text{C.0.3})$$

If we take into account that the KTP crystals belong to the crystal point group $mm2$ (orthorhombic) which reduces the d_{ij} matrix under Kleinman symmetry [55] and using the complex field amplitude definition of Equation (1.1.13), we find the simplified expression

$$\begin{pmatrix} P_x \\ P_y \\ P_z \end{pmatrix} = 2\epsilon_0 \begin{pmatrix} 0 & 0 & 0 & 0 & d_{15} & 0 \\ 0 & 0 & 0 & d_{24} & 0 & 0 \\ d_{31} & d_{32} & d_{33} & 0 & 0 & 0 \end{pmatrix} \begin{pmatrix} A_x(\omega_p)A_x(\omega_i)^* \\ A_y(\omega_p)A_y(\omega_i)^* \\ A_z(\omega_p)A_z(\omega_i)^* \\ A_y(\omega_p)A_z(\omega_i)^* + A_z(\omega_p)A_y(\omega_i)^* \\ A_x(\omega_p)A_z(\omega_i)^* + A_z(\omega_p)A_x(\omega_i)^* \\ A_x(\omega_p)A_y(\omega_i)^* + A_y(\omega_p)A_x(\omega_i)^* \end{pmatrix}. \quad (\text{C.0.4})$$

The non-linearity tensor d_{ij} shows empirical coefficients [84]:

$$\begin{aligned} d_{15} &= 1.9 \text{ pm/V}, & d_{31} &= 2.2 \text{ pm/V}, \\ d_{24} &= 4.2 \text{ pm/V}, & d_{32} &= 2.7 \text{ pm/V}, \\ & & d_{33} &= 17.4 \text{ pm/V}. \end{aligned} \quad (\text{C.0.5})$$

Considering that the signal polarization is along the z axis we neglect any coefficient not contributing. Furthermore, since we are exclusively operating at a type-II phase matching interaction, we omit any other field coefficients than d_{32} . Clearly, a stronger non-linear optical coefficient would be preferable, however, by choosing different propagation axes for idler and pump beam triples the phase mismatch. In return, the poling period Λ has to be chosen accordingly small (compare with Equation (1.4.15)) which could pose some serious fabrication issues. Nevertheless, a configuration exploiting the highest nonlinear term d_{33} is possible under the condition to increase the quasi phase-matching order m which in turn decreases the efficiency.